Viscoplastic Saffman-Taylor fingers with and without wall slip

Ariel P. Dufresne[a], Thomasina V. Ball[b], Neil J. Balmforth[a,*]

[a] *Department of Mathematics, University of British Columbia, Vancouver, BC, V6T 1Z2, Canada*
[b] *Mathematics Institute, University of Warwick, Coventry, CV4 7AL, UK*

Abstract

The Saffman-Taylor instability for the flow of a Herschel-Bulkley fluid through a Hele-Shaw cell is explored theoretically and experimentally. The theoretical analysis adopts conventional Hele-Shaw approximations, but generalized to account for a Herschel-Bulkley rheology and to include a model for the effective slip of the fluid over smooth walls. A linear stability analysis is presented for fingering instabilities on both planar and axisymmetrical interfaces. The linear instability of a planar interface is continued numerically into the nonlinear regime. It is found that certain finger widths are selected and controlled by the yield stress. Stresses also fall sufficiently behind the fingertips to allow the yield stress to block the cell to either side. Experiments are conducted using aqueous suspensions of Carbopol pumped into a Hele-Shaw cell through a circular vent. Instabilities are created by first pumping a disk of Carbopol into the cell, then either pumping air into the fluid-filled cell or withdrawing the Carbopol through the vent. In both cases, the fingers forming on the retreating air-Carbopol interface are interrogated as a function of flux, gap size and the type of cell walls. The instability is very different for cells with either rough or smooth walls, an effect that we attribute to effective slip. The trends observed in the experiments are in broad agreement with theoretical predictions.

1. Introduction

The Saffman-Taylor instability arises when a more viscous fluid is displaced by a less viscous one in a Hele-Shaw cell, leading to the invasion of distinctive fingers into the displaced fluid [1, 2]. Such fingering also arises in the displacement of viscoplastic fluids, the yield stress being unable to control the instability [3, 4, 5, 6, 7, 8, 9, 10, 11, 12, 13, 14]. Given the widespread occurrence of yield-stress fluids, this has potentially important implications in a range of industrial and environmental processes. The purpose of the current article is to present a combined theoretical and experimental exploration of this latter problem.

Our theoretical study is based on the conventional Hele-Shaw approximation for viscous fluids. This approximation employs Reynolds lubrication theory to reduce the governing equations to a reduced model based on Laplace's equation. When a complex fluid is displaced in the Hele-Shaw cell, the reduction must be generalized accordingly, with the rheology entering *via* a suitable flux-pressure-gradient relation. Here, we provide the details for a fluid modelled by the Herschel-Bulkley constitutive law, treating the displacing fluid as inviscid. Although such a viscoplastic Hele-Shaw approximation has been presented before [15, 16], we provide these details here in order to fully iron out some of the awkward wrinkles that feature in the problem and to generalize to accommodate the effective slip that many complex fluids suffer when flowing against smooth walls [17]. In particular, we exploit a recently proposed model for slip that has been experimentally calibrated [18]. Although it has been ignored or considered negligible in previous literature, any effective slip in a Hele-Shaw cell is likely to be crucial in view of the confined geometry. Indeed, part of the purpose of the present article is to establish that slip has a dramatic effect on the Saffman-Taylor instability.

With the viscoplastic version of the Hele-Shaw approximation in hand, we demonstrate through linear stability analysis that a retreating, planar interface of viscoplastic fluid is unstable and examine the impact of slip. We also consider the linear stability of retreating circular interfaces, for which the initial-value problem must be solved instead of a standard normal-mode problem. For the planar interface, we also solve the reduced model numerically to give some insight of the nonlinear development of the linear instability.

To complement theory, we conduct laboratory experiments in a Hele-Shaw cell with aqueous suspensions of Carbopol, which is commonly modelled with the Herschel-Bulkley law, even though this fluid can exhibit richer behaviour [14, 19, 20]. The set-up of the experiments is relatively simple: we first pump Carbopol into the cell through a central vent; the advancing interface displaces air and does not therefore suffer the Saffman-Taylor instability, forming a circular viscoplastic disk. We then either switch the feeder pipe to the cell and pump in air, or reverse the pump and extract the disk. Either way, as sketched in figure 1, we set up a retreating air-Carbopol interface that is prone to Saffman-Taylor fingering.

*Corresponding author: *E-mail:* njb@math.ubc.ca

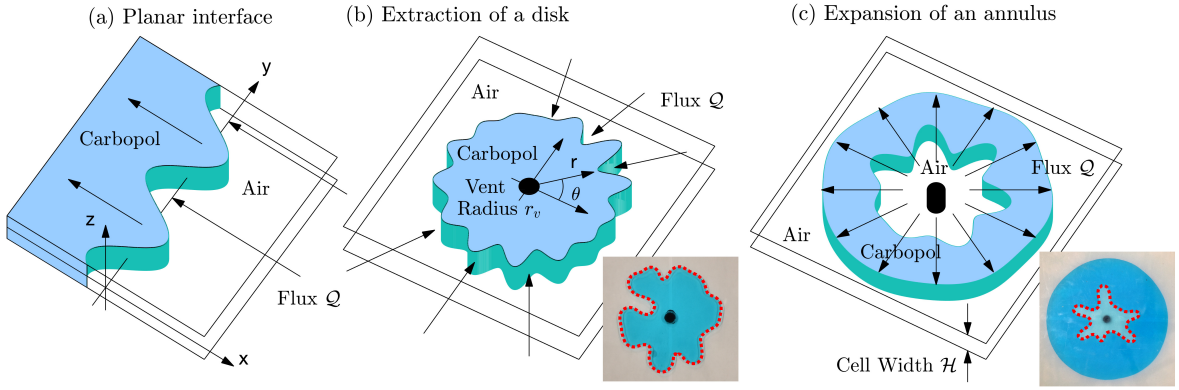

Figure 1: The geometry of the three displacement problems considered in the present paper. The inset images in (b) and (c) show photographs (from above) of experiments with a blue-coloured Carbopol suspension on smooth and rough plates respectively, as outlined in §4; the vent is visible as the central dark circle (with a radius of 2.75mm for rough plates and 3.8mm for smooth plates), and the unstable interface, as identified through image processing, is shown by the red dotted line.

To explore experimentally the impact of effective slip we use cells with either smooth or roughened walls. With smooth, plexiglass walls for our Hele-Shaw cells, the Carbopol suspension is expected to suffer slip [18]; we roughen those walls with sandpaper to try to minimize any such lubrication, following common practice in rheometry. To gauge the degree of instability and classify the finger patterns for both types of cells, we consider a number of diagnostics based on the shape of the interface observed from one side.

2. Reduced model

2.1. Formulation

Consider a two-dimensional, incompressible Herschel-Bulkley fluid between two plates with constant separation, $\mathcal{H}$. We align a Cartesian coordinate system with the midplane, so that the $z-$axis is perpendicular to the midplane, which lies along $z = 0$ (see figure 1(a)). The fluid has velocity $\boldsymbol{u} = (u, v, w)$, pressure p and deviatoric stress tensor $\boldsymbol{\tau}$. Ignoring inertia and any body forces such as gravity, conservation of mass and momentum demand that

$$\boldsymbol{\nabla} \cdot \boldsymbol{u} = 0, \tag{1}$$
$$\boldsymbol{\nabla} \cdot \boldsymbol{\tau} = \boldsymbol{\nabla} p. \tag{2}$$

The Herschel-Bulkley constitutive law is

$$\dot{\boldsymbol{\gamma}} = \boldsymbol{0}, \quad \text{if } \tau < \tau_{_Y}, \tag{3}$$
$$\boldsymbol{\tau} = \left(K\dot{\gamma}^{n-1} + \frac{\tau_{_Y}}{\dot{\gamma}} \right) \dot{\boldsymbol{\gamma}}, \quad \text{otherwise}, \tag{4}$$

where

$$\dot{\gamma}_{ij} = \frac{\partial u_i}{\partial x_j} + \frac{\partial u_j}{\partial x_i}, \qquad \dot{\gamma} = \sqrt{\tfrac{1}{2} \sum_{i,j} \dot{\gamma}_{ij}^2}, \qquad \tau = \sqrt{\tfrac{1}{2} \sum_{i,j} \tau_{ij}^2}, \tag{5}$$

and the parameters are the consistency K, power-law index n and yield stress $\tau_{_Y}$.

Along the midplane of the slot, symmetry demands that

$$w = \tau_{\mathrm{xz}} = \tau_{\mathrm{yz}} = 0 \quad \text{on } z = 0. \tag{6}$$

At the walls, $z = \pm\frac{1}{2}\mathcal{H}$, we allow the fluid to slip. In particular, we adopt the stick-slip model,

$$\begin{aligned} \begin{pmatrix} u \\ v \end{pmatrix} &= \begin{pmatrix} 0 \\ 0 \end{pmatrix}, \quad \text{if } \sqrt{{\tau_{\mathrm{xz}}}^2 + {\tau_{\mathrm{yz}}}^2} < \tau_{_W}, \\ \begin{pmatrix} \tau_{\mathrm{xz}} \\ \tau_{\mathrm{yz}} \end{pmatrix} &= \mp \left(A + \frac{\tau_{_W}}{\sqrt{u^2 + v^2}} \right) \begin{pmatrix} u \\ v \end{pmatrix}, \quad \text{otherwise}, \end{aligned} \tag{7}$$

at $z = \pm\frac{1}{2}\mathcal{H}$, where A and $\tau_{_W}$ denote material parameters describing the interaction between the fluid and walls [18].

2.2. Dimensionless equations and reduction

For a narrow slot, the gap $\mathcal{H}$ is much less than the characteristic lengthscale $\mathcal{L}$ for variations in the slot's plane: $\epsilon = \frac{\mathcal{H}}{2\mathcal{L}} \ll 1$. In this setting, the transverse velocity w must be smaller than the velocity components along the slot, u and v, by a factor of $O(\epsilon)$. Similarly, the pressure gradients driving flow must overcome the resistance stemming from the shear stresses across the slot, implying that p is larger than τ_{xz} and τ_{yz}, by a factor of $O(\epsilon^{-1})$. To bring out such features of the problem, we remove dimensions from the equations by setting

$$\begin{aligned} (x, y) = \mathcal{L}(\hat{x}, \hat{y}), \quad z = \tfrac{1}{2}\mathcal{H}\hat{z}, \quad (u, v) = \mathcal{U}(\hat{u}, \hat{v}), \\ w = \epsilon\mathcal{U}\hat{w}, \quad p = \epsilon^{-1}\mathcal{S}\hat{p}, \quad \boldsymbol{\tau} = \mathcal{S}\hat{\boldsymbol{\tau}}, \end{aligned} \tag{8}$$

where we connect the characteristic scales for stress and velocity, $\mathcal{S}$ and $\mathcal{U}$, using a characteristic viscosity μ_*:

$$\mathcal{S} = \frac{2\mu_*\mathcal{U}}{\mathcal{H}}, \quad \mu_* = K\left(\frac{2\mathcal{U}}{\mathcal{H}}\right)^{n-1}. \tag{9}$$

For the moment, we leave open the choice of the scales $\mathcal{L}$ and $\mathcal{U}$, and establish the scaling of time t when we consider the boundary conditions (which is where the dynamics enters this Stokes-flow-type problem).

After dropping the hat decoration identifying the dimensionless variables, the leading-order expression of force balance becomes

$$\begin{aligned}\frac{\partial p}{\partial x} &= \frac{\partial \tau_{\rm xz}}{\partial z} + O(\epsilon),\\ \frac{\partial p}{\partial y} &= \frac{\partial \tau_{\rm yz}}{\partial z} + O(\epsilon),\\ \frac{\partial p}{\partial z} &= O(\epsilon).\end{aligned} \tag{10}$$

Evidently,

$$\begin{pmatrix}\tau_{\rm xz}\\ \tau_{\rm yz}\end{pmatrix} = z\boldsymbol{\nabla} p + O(\epsilon). \tag{11}$$

The yielded part of the constitutive law becomes

$$\boldsymbol{\tau} = \frac{\dot\gamma^n + \mathrm{Bi}}{\dot\gamma}\begin{pmatrix} 2\epsilon u_x & \epsilon(u_y+v_x) & u_z+\epsilon^2 w_x\\ \epsilon(u_y+v_x) & 2\epsilon v_y & v_z+\epsilon^2 w_y\\ u_z+\epsilon^2 w_x & v_z+\epsilon^2 w_y & -2\epsilon w_z\end{pmatrix}, \tag{12}$$

for $\tau \geq \mathrm{Bi}$, where the dimensionless yield stress, or Bingham number, is

$$\mathrm{Bi} = \frac{\tau_{_Y}}{\mathcal{S}} = \frac{\mathcal{H}\tau_Y}{2\mu_*\mathcal{U}}, \tag{13}$$

and we have used a shorthand subscript notation on (u, v, w) in place of partial derivatives. At the walls, the slip law becomes

$$\begin{pmatrix}\tau_{\rm xz}\\ \tau_{\rm yz}\end{pmatrix} = \mp\left(\frac{\mathcal{U}A}{\mathcal{S}} + \frac{\mathrm{B_w}}{\sqrt{u^2+v^2}}\right)\begin{pmatrix}u\\ v\end{pmatrix}, \quad \text{at } z=\pm 1, \tag{14}$$

if $\sqrt{{\tau_{\rm xz}}^2 + {\tau_{\rm yz}}^2} \geq \mathrm{B_w}$, where

$$\mathrm{B_w} = \frac{\tau_{_W}}{\mathcal{S}} \equiv \frac{\tau_{_W}}{\tau_{_Y}}\mathrm{Bi}. \tag{15}$$

We assume that $\tau_{_W} < \tau_{_Y}$, and so $\mathrm{B_w} < \mathrm{Bi}$.

2.3. The flow pattern

2.3.1. Strongly sheared regions

The form of the deformation tensor on the right of equation (12) suggests that the stress tensor $\boldsymbol{\tau}$ is dominated by the components $\tau_{\rm xz}$ and $\tau_{\rm yz}$. Therefore, provided that $\tau^2 \approx {\tau_{\rm xz}}^2 + {\tau_{\rm yz}}^2$ exceeds Bi^2, we have $\dot\gamma \approx \sqrt{u_z^2+v_z^2}$ and

$$z\boldsymbol{\nabla} p = \begin{pmatrix}\tau_{\rm xz}\\ \tau_{\rm yz}\end{pmatrix} = \left(\dot\gamma^{n-1} + \frac{\mathrm{Bi}}{\dot\gamma}\right)\begin{pmatrix}u_z\\ v_z\end{pmatrix}. \tag{16}$$

That is,

$$\begin{pmatrix}u_z\\ v_z\end{pmatrix} = (|z|-Y)^{\frac{1}{n}} S^{\frac{1}{n}-1}\boldsymbol{\nabla} p\,\mathrm{sgn}(z), \tag{17}$$

where

$$S = |\boldsymbol{\nabla} p| = \sqrt{p_x^2+p_y^2}, \qquad Y = \frac{\mathrm{Bi}}{S}. \tag{18}$$

Evidently, $1 > |z| > Y$ for such a solution to exist. Provided that one does, the velocity profile over this region can be found by integrating (17), subject to the conditions

$$\left.\begin{pmatrix}u\\ v\end{pmatrix}\right|_{z=\pm 1} \equiv \begin{pmatrix}U\\ V\end{pmatrix} = -\frac{\Sigma}{(2+\frac{1}{n})}\mathrm{Max}\left(0, S-\mathrm{B_w}\right)\frac{\boldsymbol{\nabla} p}{S}, \tag{19}$$

where

$$\Sigma = (2+\tfrac{1}{n})\frac{\mathcal{S}}{\mathcal{U}A} \equiv (2+\tfrac{1}{n})\frac{2\mu_*}{\mathcal{H}A}. \tag{20}$$

It further follows that the slot-averaged flux is

$$\begin{aligned}\frac{1}{2}\int_{-1}^{1}\begin{pmatrix}u\\ v\end{pmatrix}\mathrm{d}z &= \begin{pmatrix}U\\ V\end{pmatrix} - \int_0^1 z\begin{pmatrix}u_z\\ v_z\end{pmatrix}\mathrm{d}z &(21)\\ &= -(2+\tfrac{1}{n})^{-1}\frac{Q}{S}\boldsymbol{\nabla} p - \int_0^Y z\begin{pmatrix}u_z\\ v_z\end{pmatrix}\mathrm{d}z, &(22)\end{aligned}$$

where

$$\begin{aligned}Q(S) =& \Sigma\ \mathrm{Max}\left(0, S-\mathrm{B_w}\right)\\ &+ \left(1+\frac{nY}{n+1}\right)S^{\frac{1}{n}}\left[\mathrm{Max}(0,1-Y)\right]^{\frac{1}{n}+1}.\end{aligned} \tag{23}$$

2.3.2. The pseudo-plug

In $|z| < Y$, the preceding solution is no longer valid, and the approximation $\tau^2 \approx {\tau_{\rm xz}}^2 + {\tau_{\rm yz}}^2$ motivated by the form of $\dot{\boldsymbol{\gamma}}$ in (16) seemingly suggests that $\tau < \mathrm{Bi}$, implying we must take $(u_z, v_z) \to 0$. However, this conclusion is false because if u_z and v_z both become small, and in particular $O(\epsilon)$, then $\dot\gamma = O(\epsilon)$ and all components of $\boldsymbol{\tau}$ become of similar order in view of the factor $\mathrm{Bi}/\dot\gamma$ stemming from the yield stress term in (12). In other words, once $z \to \pm Y$ and $(u_z, v_z) \to O(\epsilon)$, we must instead take

$$\begin{aligned}u &= u_0(x,y,t) + \epsilon u_1(x,y,z,t) + ...\\ v &= v_0(x,y,t) + \epsilon v_1(x,y,z,t) + ...,\end{aligned} \tag{24}$$

leading to

$$\begin{aligned}\dot\gamma &\approx \epsilon\sqrt{\Gamma^2 + u_{1z}^2 + v_{1z}^2},\\ \Gamma^2 &= 2u_{0x}^2 + 2v_{0y}^2 + 2(u_{0x}+v_{0y})^2 + (u_{0y}+v_{0x})^2\end{aligned} \tag{25}$$

and

$$\boldsymbol{\tau} = \frac{\mathrm{Bi}}{\sqrt{\Gamma^2+u_{1z}^2+v_{1z}^2}}\begin{pmatrix}2u_{0x} & u_{0y}+v_{0x} & u_{1z}\\ u_{0y}+v_{0x} & 2v_{0y} & v_{1z}\\ u_{1z} & v_{1z} & 2w_{0z}\end{pmatrix}, \tag{26}$$

with $w_0 = -z(u_{0x}+v_{0y})$. Because the (dimensional) deviatoric stress is now given by $\tau \approx \tau_{_Y}\dot{\boldsymbol{\gamma}}/\dot\gamma$, the region $-Y < z < Y$ can be viewed as a perfectly plastic (von Mises) material that, despite $\tau_{\rm xz}$ and $\tau_{\rm yz}$ continuing to be prescribed by $z\boldsymbol{\nabla} p$, actually remains yielded because of the other components of the stress tensor. Indeed, one may solve

$$z\boldsymbol{\nabla} p = \frac{\mathrm{Bi}}{\sqrt{\Gamma^2+u_{1z}^2+v_{1z}^2}}\begin{pmatrix}u_{1z}\\ v_{1z}\end{pmatrix}, \tag{27}$$

for the shear rates, u_{1z} and v_{1z}, in terms of the in-plane deformation rate, Γ [21]. Nevertheless, the flow profile $-Y < z < Y$ is plug-like, in view of (24), leading to Walton & Bittleston's use of the terminology "pseudo-plug." Only when u_0 and v_0 turn out to be independent of position does the pseudo-plug develop into a true plug [22, 23]. Consequently, since $(u_z, v_z) = O(\epsilon)$, we may discard the final integral in (22), to arrive at the flux gradient relation defined by the function $Q(S)$ in (23).

2.3.3. The fake yield surfaces

The pseudo-plug is connected to the sheared regions across the "fake" surfaces, $z = \pm Y$. This connection actually takes place over a thin layer of thickness δ, where

$$z = \pm(Y+\delta\zeta), \quad \begin{bmatrix} u \\ v \end{bmatrix} \sim \begin{bmatrix} u_0(x,y,t) \\ v_0(x,y,t) \end{bmatrix} + \delta^{\alpha+1} \begin{bmatrix} \mho(x,y,\zeta,t) \\ \Upsilon(x,y,\zeta,t) \end{bmatrix}. \tag{28}$$

To relate δ to ϵ and determine the power α, we insert these relations into (16) (using the full form of $\dot\gamma$). Then,

$$\begin{aligned} &\left[(\epsilon^2\Gamma^2 + \delta^{2\alpha}\Delta^2)^{n/2} + \mathrm{Bi}\right]^2 \frac{\delta^{2\alpha}\Delta^2}{\epsilon^2\Gamma^2 + \delta^{2\alpha}\Delta^2} \\ &= z^2 S^2 = \left(1 + \delta\frac{\zeta}{Y}\right)^2 \mathrm{Bi}^2, \end{aligned} \tag{29}$$

where

$$\Delta = \sqrt{\mho_\zeta^2 + \Upsilon_\zeta^2}. \tag{30}$$

Provided $\delta^{2\alpha} \gg \epsilon^2$, both sides of this equation equal Bi^2 to leading order. Equating the three next-order terms implies

$$\delta S\zeta = \delta^{n\alpha}\Delta^n - \frac{\epsilon^2 \mathrm{Bi}\Gamma^2}{2\delta^{2\alpha}\Delta^2}. \tag{31}$$

Hence,

$$\alpha = n^{-1}, \quad \delta = \epsilon^{\frac{2n}{n+2}} \quad \text{and} \quad S\zeta = \Delta^n - \frac{\mathrm{Bi}\Gamma^2}{2\Delta^2}, \tag{32}$$

which confirm that $\delta^{2\alpha} \equiv \epsilon^{\frac{4}{n+2}} \gg \epsilon^2$. The final algebraic equation for $\Delta(\zeta)$ in (32) bridges between the limit of the pseudo-plug solution,

$$\Delta \sim \Gamma\sqrt{\frac{Y}{2|\zeta|}},$$

following from (27), for $\zeta \to -\infty$, to the limit of the solution for the strongly sheared region,

$$\Delta \sim (S\zeta)^{\frac{1}{n}}$$

given by (17), for $\zeta \to \infty$. Because the bridge arises across a narrow region of $O(\epsilon^{\frac{2n}{n+2}})$, the contribution to the flux in (22) can be ignored.

2.4. The flux-gradient relation

An integral of the mass conservation equation across the slot implies that

$$\frac{\partial}{\partial x}\int_{-1}^{1} u \,\mathrm{d}x + \frac{\partial}{\partial y}\int_{-1}^{1} v \,\mathrm{d}y = 0. \tag{33}$$

Hence, using (22), we arrive at

$$\boldsymbol{\nabla}\cdot\mathbf{q} = 0, \qquad \mathbf{q} = \begin{pmatrix} q_\mathrm{x} \\ q_\mathrm{y} \end{pmatrix} = -\frac{Q(S)}{S}\boldsymbol{\nabla}p, \tag{34}$$

where $|\mathbf{q}| = Q(S)$ is the flux-gradient relation given by (23), which we now repeat, but in the slightly different form,

$$\begin{aligned} Q(S) = {} & \Sigma\,\mathrm{Max}\,(0, S - \mathrm{B_w}) \\ & + \frac{1}{S^2}\left(S + \frac{n\mathrm{Bi}}{n+1}\right)[\mathrm{Max}(0, S - \mathrm{Bi})]^{\frac{1}{n}+1}. \end{aligned} \tag{35}$$

This relation recovers that derived in [14, 16] when $\Sigma \to 0$, which corresponds to eliminating any slip over the walls. If we further take $\mathrm{Bi} = 0$, we emerge with the flux-gradient relation for a power-law fluid, and when, in addition, $n = 1$, we arrive at the Newtonian law $Q(S) = S$. The relations with and without slip are illustrated in figure 2 for parameter settings typical of the experiments we report later. In the circular geometry for which we conduct those experiments, the imposition of a constant flux through the slot from a source or sink at the centre actually implies that Q varies with radial position. The fluid therefore progresses along an entire section of the flux-gradient relation in its passage through the cell; excursions for expanding or extracted axisymmetrical flow are indicated in figure 2.

The full flux-gradient relation contains two switches: if $S < \mathrm{B_w} < \mathrm{Bi}$, equivalent to ${\tau_{\mathrm{xz}}}^2 + {\tau_{\mathrm{yz}}}^2 < {\mathrm{B_w}}^2 < \mathrm{Bi}^2$ at $z = \pm 1$, the fluid is not sufficiently stressed to either slip over the walls or deform between them. Instead, a stagnant plug bridges across the gap. On the other hand, $S > \mathrm{Bi} > \mathrm{B_w}$, then $\mathrm{Bi}^2 < {\tau_{\mathrm{xz}}}^2 + {\tau_{\mathrm{yz}}}^2$ at $z = \pm 1$, and the shear stresses are sufficient to force the fluid to both slide over walls and shear internally against those boundaries, with a pseudo-plug occupying a section surrounding the midplane. The situation $\mathrm{Bi} > S > \mathrm{B_w}$ corresponds to a stress state with $\mathrm{Bi}^2 < {\tau_{\mathrm{xz}}}^2 + {\tau_{\mathrm{yz}}}^2$ at $z = \pm 1$. In this case, sliding must occur, but the shear stresses are not sufficient to generate any internal shear adjacent to the walls. The interpretation is that the pseudo-plug now fills the entire slot with $(U, V) \equiv (u_0, v_0)$. Unless the sliding velocity is independent of position, the fluid does not slide as a rigid block, and the in-plane stress components contribute to holding the fluid just above the yield stress, as in §2.3.2. The flux-gradient relation $Q = \Sigma\,\mathrm{Max}\,(0, S - \mathrm{B_w})$ that applies for $\mathrm{Bi} > S > \mathrm{B_w}$ is, coincidentally, equivalent to the simplified forms for flow with no-slip adopted by Coussot [3] and Alexandrou & Entov [24]. Figure 2 highlights how the fluid flow through the Hele-Shaw cells of the experiments can take place entirely due to sliding where the

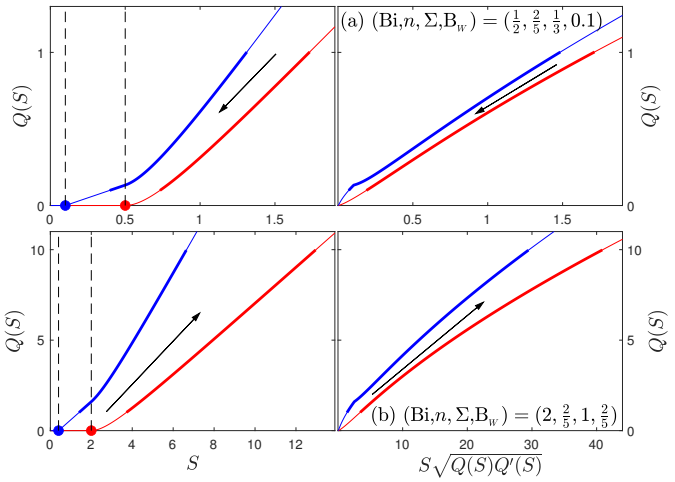

Figure 2: The flux gradient relation in (35) illustrated for the parameter settings indicated and experiments with (a) expanding or (b) extracted axisymmetrical flow from a source or sink at the centre of the cell. The red and blue curves indicate the cases without ($\Sigma = 0$) or with ($\Sigma > 0$) wall slip, respectively. The switches at $S = \mathrm{Bi}$ and $S = \mathrm{B_w}$ are indicated. The thicker sections of the curves indicate the excursion taken by fluid expanding or retreating axisymmetrically; in each case, in the experiments an interface is positioned initially at a radial location corresponding to $Q = 1$. On the right, we show the corresponding plots of the quantity $S\sqrt{Q(S)Q'(S)}$, which controls the basic linear instability (see §3.1).

fluxes are lowest, and partly by sliding where the fluxes are highest, unless slip is removed.

Note that the form of the flux-gradient relation relies on the assumption that the sliding parameter Σ is $O(1)$. Had this parameter instead been $O(\epsilon^{-2})$, then the magnitude of the slip velocity would have violated our asymptotic scalings, and the implied in-plane stresses could no longer be discarded in the leading-order force balance equations (10). A revision of the asymptotic reduction would then be demanded, more like that followed to describe free viscous or viscoplastic films [25, 26, 27, 28, 29, 30].

2.5. Boundary conditions

In the Saffman-Taylor problem equation (34) must be supplemented with the conditions holding at the fluid interface, $x = X(y,t)$. Assuming that this interface maintains a constant curvature across the slot (with associated dynamic contact lines), we have an approximate kinematic condition,

$$X_t + q_{\mathrm{y}} X_y = q_{\mathrm{x}}, \tag{36}$$

and Laplace-Young relation,

$$p(X,y,t) = P_{amb} - \sigma\mathcal{K} \tag{37}$$

where P_{amb} denotes the pressure beyond the fluid, $\mathcal{K}$ denotes the interface curvature and σ is a parameter that is related to the dimensional surface tension σ_* by

$$\sigma = \frac{\sigma_* \mathcal{H}}{2\mathcal{L}^2 \mathcal{S}}. \tag{38}$$

To arrive at (36), the dimensional time must be scaled by $(2+\frac{1}{n})\mathcal{L}/\mathcal{U}$, given that our non-dimensionalization of the problem implies that the average velocity across the slot is $(2+\frac{1}{n})^{-1}\mathcal{U}(q_{\mathrm{x}}, q_{\mathrm{y}})$.

Finally, the fluid must be driven through the slot by imposing a flux condition. In the planar problem, if the net dimensional flow speed down the slot is $\mathcal{V}$, then we choose $\mathcal{U} = (2+\frac{1}{n})^{-1}\mathcal{V}$ (implying that the net dimensionless flux is unity). We further select $\mathcal{L}$ to be a typical finger scale, adopting periodic boundary conditions in y. The interfacial curvature is given by

$$\mathcal{K} = \mathcal{K}_0 + \frac{X_{yy}}{(1+X_y^2)^{\frac{3}{2}}}, \tag{39}$$

where $\mathcal{K}_0$ denotes the constant component associated with the local meniscus.

For problems with circular geometry, we may force fluid through the cell by imposing a flux $\mathcal{Q}$ through a vent of radius r_v. Transforming to the curvilinear coordinates (r,θ), we set $\mathbf{q} = (q_{\mathrm{r}}, q_\vartheta)$ and write (34) and (36) in the alternative forms,

$$\frac{1}{r}\frac{\partial}{\partial r}(r q_{\mathrm{r}}) + \frac{1}{r}\frac{\partial q_\vartheta}{\partial \theta} = 0, \tag{40}$$

$$R_t + q_\vartheta R_\theta = q_{\mathrm{r}} \text{ at } r = R(\theta,t). \tag{41}$$

We may then take $\mathcal{L} = r_o$, the initial radial position of the interface, and impose the net radial velocity $q_{\mathrm{r}} = 1$ at $r = 1$. This corresponds to fixing $\mathcal{U} = (2+\frac{1}{n})\mathcal{Q}/[2\pi r_o \mathcal{H}]$. In this case, the interface, at $r = R(\theta,t)$, has curvature [31],

$$\mathcal{K} = \mathcal{K}_0 + \frac{R^2 + 2R_\theta^2 - RR_{\theta\theta}}{(R^2+R_\theta^2)^{\frac{3}{2}}}. \tag{42}$$

For an expanding interface, $r_o \gtrsim r_v$, but for a retreating interface, $r_v \ll r_o$, suggesting that any lengthscale based on r_v should be irrelevant (motivating the selection $\mathcal{L} = r_o$).

For the circular problem, we may also supplement an inner, retreating interface with a second, outer interface to model the expanding viscoplastic annulus shown in figure 1(c). This problem was considered explicitly in [14], and we avoid any detailed additional discussion here. We do, however, use the analysis in [14] to provide predictions from linear stability theory for expanding annuli in §4.

Adopting the interfacial conditions in (36)-(37) along with (39) or (42) is common practice in theory for Hele-Shaw cells (e.g. [1, 2, 32, 31]). However, this approximation can lead to quantitative errors in the modelling [2, 33]. Indeed, when air is displaces Carbopol in a Hele-Shaw cell with no-slip plates, residual layers of Carbopol may be left behind, features that were observed in the experiments we report later with roughened plates. By contrast, no such residual layers of air were observed when the Carbopol displaced air. In the current theory, we adopt (36)-(37) largely for simplicity, although the residual layers of Carbopol observed experimentally were relatively thin and did not appear to significantly impact displacements.

3. Planar fingers

With the reduced model in hand, we may explore the dynamics of viscoplastic Saffman-Taylor fingers. We first consider this problem for a planar interface, before turning to circular geometry. In the planar problem, we choose the domain length in y to be 2π (so that $\mathcal{L}$ is selected as the wavelength of the most significant finger), and consider the moving domain $\varsigma t \le x \le X = \varsigma t + \hat{X}(y,t)$, where $\varsigma = \pm 1$, for a problem with an advancing or retreating interface. The kinematic condition (36) then translates to $\hat{X}_t + q_{\rm y}\hat{X}_y = q_{\rm x} - \varsigma$, whereas we impose the flux condition $q_{\rm x} = 1$ at $x = \varsigma t$.

3.1. Linear instability

The solution for a steadily advancing planar interface is given by

$$\begin{aligned} &X = X_0(t) = X_0(0) + \varsigma t, \quad (q_{\rm x}, q_{\rm y}) = (\varsigma, 0), \\ &Q = 1, \quad p = \varsigma S_0(X_0 - x), \quad S = S_0, \end{aligned} \tag{43}$$

where S_0 is the pressure gradient required to drive the background flux, $Q_0 = Q(S_0)$. For the planar problem, we may choose characteristic scales so that $Q_0 = 1$, as stated above. However, in the circular problem, the background flux varies with radial position. For a comparison with that problem, we therefore avoid introducing this particular choice.

Considering small perturbations about the planar state, we set

$$X = X_0(t) + \hat{X}_\ell(t)e^{i\ell y}, \quad p = \varsigma S_0(X_0 - x) + p_\ell(x,t)e^{i\ell y}, \tag{44}$$

where $\ell = 1, 2, ...,$ is the wavenumber, and then discard terms in the equations of the reduced model that are nonlinear in the amplitudes $\hat{X}_\ell$ and p_ℓ. We first arrive at the relations,

$$S = S_0 - \varsigma \frac{\partial p_\ell}{\partial x} e^{i\ell y}, \tag{45}$$

$$(q_{\rm x}, q_{\rm y}) = (\varsigma Q_0, 0) - \left(Q'(S_0)\frac{\partial p_\ell}{\partial x}, \frac{i\ell Q_0}{S_0} p_\ell \right) e^{i\ell y}, \tag{46}$$

which then imply

$$\frac{\partial^2 p_\ell}{\partial x^2} = \frac{\ell^2 Q_0 p_\ell}{S_0 Q'(S_0)}, \tag{47}$$

or

$$p_\ell = A(t) \exp\left[\ell (x - X_0) \sqrt{\frac{Q_0}{S_0 Q'(S_0)}} \right], \tag{48}$$

for some $A(t)$, if we assume that the viscoplasic fluid extends to $x \to -\infty$. From the developments of (36) and (37), we then find

$$\frac{{\rm d}\hat{X}_\ell}{{\rm d}t} = -\ell A \sqrt{\frac{Q_0 Q'(S_0)}{S_0}} \quad \text{and} \quad A - \varsigma S_0 \hat{X}_\ell = \sigma \ell^2 \hat{X}_\ell. \tag{49}$$

Hence,

$$\hat{X}_\ell(t) = \hat{X}_\ell(0) \exp\left[-\ell \sqrt{\frac{Q_0 Q'(S_0)}{S_0}} (\varsigma S_0 + \sigma \ell^2) t \right]. \tag{50}$$

As long as the flux-gradient relation is always increasing ($Q'(S) > 0$, which is the case for the constitutive laws considered here, as illustrated in figure 2), the advancing interface is therefore always stable; the retreating interface is unstable to the ℓ^{th} mode if $S_0 > \sigma \ell^2$.

Equation (50) predicts a most unstable wavelength given by $2\pi\sqrt{3\sigma/S_0}$, with a growth rate equal to $\frac{2}{3} S_0 \sqrt{Q_0 Q(S_0)'/3\sigma}$. The factor, $S_0\sqrt{Q_0 Q'(S_0)}$, indicates how the rheology enters the linear problem to impact stability. Notably, as highlighted by figure 2, the addition of slip leads to a reduction in this factor, suggestive of a corresponding reduction in the degree of instability for our experiments. Also, in the limit $Q_0 \to 0$ without slip, we must have $S_0 \to {\rm Bi}$, implying that the dimensional, most unstable wavelength is proportional to $\sqrt{\sigma_* \mathcal{H}/\tau_Y}$ (*cf.* [3]). Similarly with slip, when $S_0 \to {\rm B_w}$, the dimensional most unstable wavelength is proportional to $\sqrt{\sigma_* \mathcal{H}/\tau_w}$. More generally, the prediction in (49) can be compared with experimental results in planar geometry. Further analysis is necessary for circular geometry, however, in view of the time dependence of the axisymmetric flow [14].

3.2. Nonlinear fingers

3.2.1. Numerical scheme

To look at the initial development of unstable viscoplastic Saffman-Taylor fingering, we solve (34), (36) and (37) numerically for Bingham fluid ($n = 1$) beginning from the initial condition, $\hat{X}(y,0) = 20 + 10^{-2}\cos y$ (the choice of 20 for the mean position ensures that the boundary at $x = -t$ plays no role in the dynamics).

To solve (34) at each instant of time, and given the current position of the interface, we first map the domain into a fixed rectangle by introducing the variable $\xi = (x - \varsigma t)/(X - \varsigma t) = (x - \varsigma t)/\hat{X}$. We then adopt a fixed grid in y and use the fast Fourier transform to evaluate spatial derivatives in that direction. This turns (34) into a set of coupled ODEs in ξ, that can be solved using MATLAB's in-built solver bvp5c. The grid in y has 64 or 128 points; bvp5c introduces an adaptive grid with a variable number of points for ξ. To accelerate the computations we also exploit the reflection symmetry about $y = \pi$ to further halve the grid in y.

In solving (34), we also smooth the switch in the flux-pressure-gradient relation at $Q = 0$ by replacing $Q(S)$ in (34) by $\sqrt{Q^2 + \varepsilon S^2}$, where ε is a small regularization parameter. Practically, ε is chosen to be 10^{-2} or smaller, and the effect of this regularization is gauged by varying the precise value. The regularization also leads to a prescribed pressure solution over any true plugs, which would otherwise be indeterminate.

With the solution for the pressure in hand, we construct the flux at the interface, and then advance the interface position $x = X(y,t)$ in time, using (36). For this task, we employ MATLAB's implicit integrator, ode15s.

Note that the mapping $\xi = (x - \varsigma t)/\hat{X}$ implicitly limits the numerical strategy to fingers that do not thin behind the advancing finger tip. *i.e.* to interfacial shapes for which $x = X(y,t)$ is single valued. For the Newtonian problem, it is known that fingers can develop such thinned sections at late times [34, 35]. Such shapes are inaccessible for the current numerical scheme and the computation is necessarily stopped when X_y becomes too large.

3.2.2. Solutions without slip

Figures 3 and 4 compare numerical solutions for retreating interfaces of Newtonian ($\mathrm{Bi} = \Sigma = 0$) and non-slipping Bingham ($\mathrm{Bi} = 2$, $\Sigma = 0$) fluid. For the two solutions, the surface tension parameter is chosen so that only the first ($\ell = 1$) Fourier mode in y is unstable ($\sigma = 0.5$ for $\mathrm{Bi} = 0$, and $\sigma = 1$ for $\mathrm{Bi} = 2$). The development of Saffman-Taylor instability on the interface is similar between the two solutions with the interface deforming into a growing finger. The main difference between the two solutions is that, for the Bingham case, the flux falls significantly adjacent to the rearward portions of the interface, with the stress decreasing to the yield stress there. The progress of the lagging parts of the interface thereby become arrested, and fluid retreats only along the front of the finger. For the Newtonian case, instead, the interface slows at the back, but does not halt.

A main feature of the numerical solutions in figures 3 and 4 is the lengthening of the interface $x = X(y,t)$ along the sides of the finger, which become relatively flat. The mapping used to solve (34) on a rectangular domain becomes problematic in this situation, with the limited spatial resolution prompting the development of short-wavelength oscillations in y. We terminate the computations before these spurious features become too severe, but they are visible in some of the final solutions shown in the figures, particularly in the yield surface of the Bingham cases.

Alexandrou & Entov [24] have previously given solutions for the advance of a finger of inviscid fluid at constant speed into a cell filled with a (miscible) yield-stress fluid. As mentioned earlier, however, these authors exploit an approximation of the flux-gradient relation that is more similar to the purely sliding law we have derived here (*i.e.* (35) with $\mathrm{Bi} \to \infty$). Nevertheless, their solution possesses plugs on either side of the advancing finger, somewhat like those seen in figure 4(a). The development of the blocked section of the cell along the lines $y = 0$ and 2π is shown in more detail in figure 4(c). The retreat of the yield surface here appears to match that of the interface at late times, suggesting that the solution may indeed converge to a steadily translating form.

Further evidence for such convergence is shown in figure 5, which presents solutions with varying Bingham numbers, holding all other parameters fixed. Plotted are snapshots of the interface in the frame of the fingertips; *i.e.* after shifting the origin to $(x,y) = (X_{tip}, \pi)$ where $X_{tip}(t) = \mathrm{Min}(X)$. This shift increasingly collapses the profile of the fingertips near $x = X_{tip}$ as time progresses, suggesting the convergence to a steadily propagating form. The profiles also highlight how the finger widths Δ and speed of advance v_{tip} depend on Bingham number, with the finger narrowing and becoming faster as the yield stress increases. In figure 5, the width is estimated by measuring where the yield surface intersects the interface for each final solution.

The limiting tip speed and finger width are connected since in any steadily translating final state, mass conservation demands that $\Delta v_{tip} = \pi$. As the plug is still in expansion at the end of the computations and the fingertip is accelerating, the measurements of v_{tip}^{-1} and Δ/π plausibly bracket the limiting relative finger width (the viscoplastic analogue of Saffman & Taylor's λ parameter). Evidently, with surface tension, a particular finger width is selected, as found previously in the Newtonian problem [2, 34, 35, 36]. Here, the finger width is further controlled by the yield stress, which constricts the fingers and lowers the relative width Δ/π below $\frac{1}{2}$, the bound encountered in the Newtonian problem for $\sigma \to 0$.

Figure 5 also highlights another feature of the finger solutions, namely that scaling the interface position by the finger width Δ leads to some collapse of all the profiles. This scaling is equivalent to that noted by Pitts [37] in the Newtonian Saffman-Taylor problem. In the current viscoplastic problem, we may rationalize this observation by noting that when the finger becomes relatively thin and surrounded by a plug, the domain adopted in y must become secondary in setting the finger profile, raising the question of what lengthscale sets the width. The key points are that the pressure gradient S must remain $O(\mathrm{Bi})$ in order to drive the finger forward, so $p \sim S\Delta \sim \mathrm{Bi}\Delta$, whereas the capillary stress demands that the pressure is $p \sim \sigma\Delta^{-1}$. Thus, $\Delta \sim \sqrt{\sigma/\mathrm{Bi}}$, and since this prescribes the only relevant lengthscale, a collapse is implied by the scaling of the profile by Δ. The scaling of Δ with $\mathrm{Bi}^{-\frac{1}{2}}$ is indeed observed for the solutions shown in figure 5 (see the inset panel on the right). In dimensional terms, because our surface tension parameter is given by (38), we conclude that the finger width is set by the lengthscale $\sqrt{\sigma_* \mathcal{H}/\tau_Y}$, which also corresponds to the wavelength of the most unstable mode in the plastic limit (see §3.1; [3]).

3.2.3. Slippy solutions

Numerical solutions including slip are shown in figure 6; again, the surface tension parameter is chosen so that only the $\ell = 1$ mode is unstable. For the solution shown at the top of figure 6(a), the slip parameter Σ is set to a value so that the viscoplastic fluid is internally yielded when it is uniformly withdrawn from the cell (*i.e.* $S_0 > \mathrm{Bi}$). However, although the fluid is consequently internally yielded to begin with, once an unstable finger develops, the

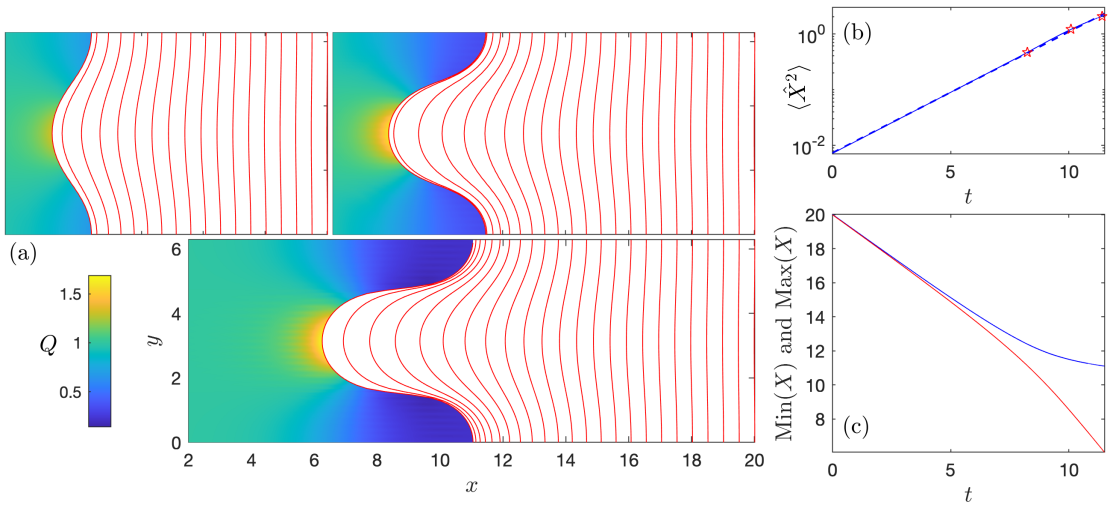

Figure 3: Numerical solution for a retreating, planar interface of Newtonian fluid ($n = 1$, Bi $= \Sigma = 0$; $\sigma = 0.5$). In panel (a), we display three snapshots of the flux $Q(x, y, t)$, together with a succession of the equally spaced previous snapshots of the retreating interface $x = \hat{X}(y, t)$ (equally spaced by 0.5). The panels on the right show time series of (b) $\langle \hat{X}^2 \rangle$ (angular brackets denoting a spatial average) and (c) the maximum (blue) and minimum (red) interface positions. In (b), the dashed lines show the expected linear growth and the stars indicate the times of the snapshots of Q shown in (a).

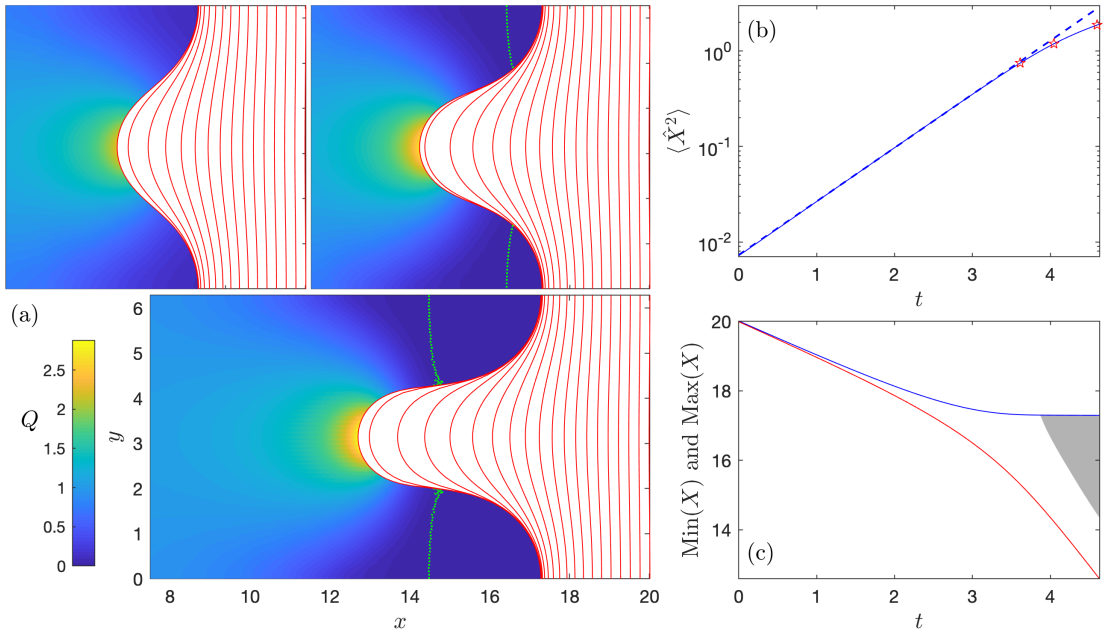

Figure 4: Numerical solutions for a retreating interface of non-slipping Bingham fluid ($n = 1$, Bi $= 2$, $\Sigma = 0$; $\sigma = 1$). Three snapshots of $Q(x, y, t)$ are again displayed in (a), along with previous interface positions (equally spaced by 0.25). The dotted (green) contours show the yield surfaces. The panels on the right show time series of (b) $\langle \hat{X}^2 \rangle$ and (c) the maximum (blue) and minimum (red) interface positions. In (b), the dashed lines show the expected linear growth and the stars indicate the times of the snapshots of Q shown in (a). In (c), the shaded region shows the extent of the growing plug along $y = 0$ and 2π.

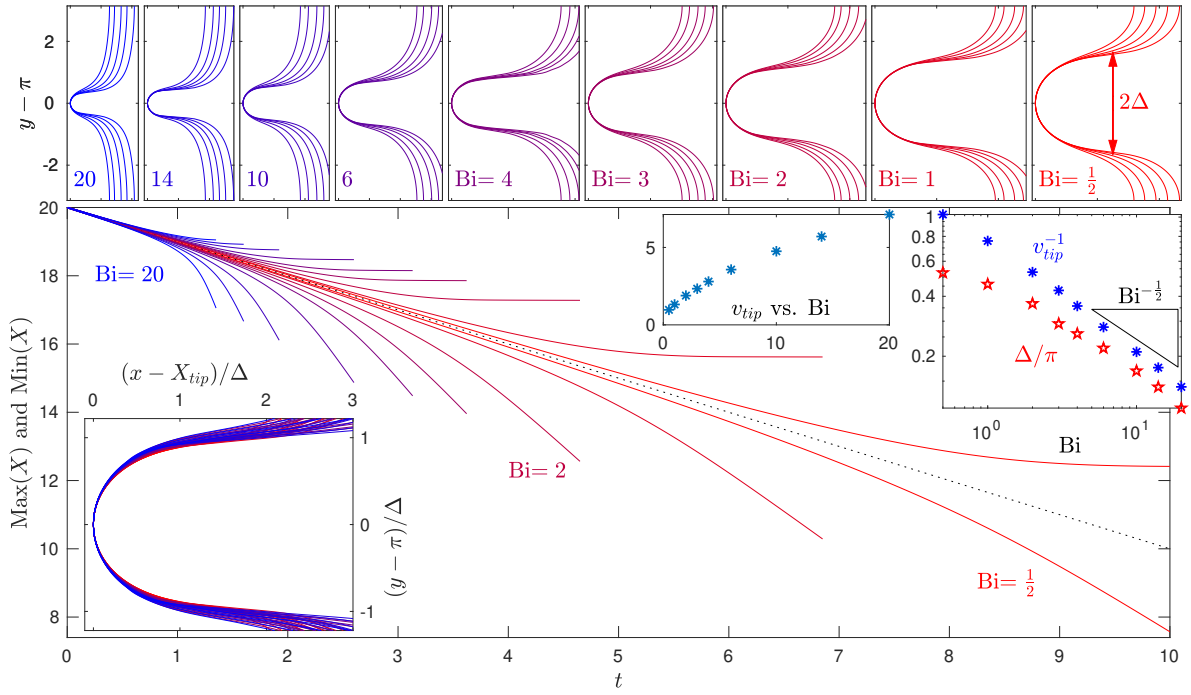

Figure 5: Numerical solutions for a retreating interface of non-slipping Bingham fluid ($n = 1$, $\Sigma = 0$; $\sigma = 1$) with varying Bi (as indicated). Snapshots of the interface in the frame of reference of the finger tip are shown in the top row (*i.e.* in the frame with origin at $(x, y) = (X_{tip}, \pi)$ where $X_{tip} = \mathrm{Min}(X)$). The snapshots are roughly equally spaced by intervals equal to a fiftieth of the final time in each computation. The lower panel shows the times series of $\mathrm{Min}(X)$ and $\mathrm{Max}(X)$ for all the solutions. The lower left inset shows the profiles of the all the finger tips, rescaled by the finger width Δ, defined as the vertical distance between the final yield points on the interface. The right-hand insets show the final speed of the fingertips v_{tip}, then its inverse and Δ/π against Bi.

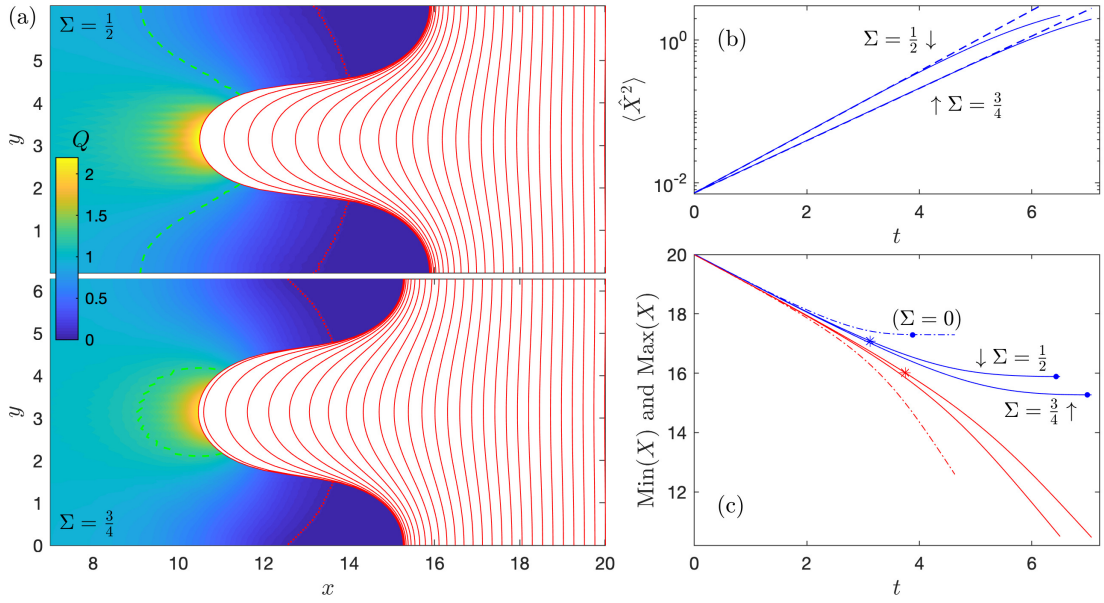

Figure 6: Numerical solutions for a retreating interface of slipping Bingham fluid ($n = 1$, Bi $= 2$) with $(\Sigma, \sigma) = (\frac{1}{2}, \frac{2}{5})$ (top) and $(\Sigma, \sigma) = (\frac{3}{4}, \frac{2}{3})$ (bottom); $\mathrm{B_w} = \frac{1}{5}\mathrm{Bi}$. In (a), the final solution for $Q(x, y, t)$ is plotted along with a succession of previous interface positions (equally spaced by 0.25). The dashed (green) contours show the internal yield surfaces where $S = \mathrm{Bi}$; the (red) dotted lines show the contours $Q = 0.1$. The panels on the right show time series of (b) $\langle \hat{X}^2 \rangle$ and (c) the maximum (blue) and minimum (red) interface positions. In (b), the dashed lines show the expected linear growth. In (c), the solution from figure 4 is shown by the dash-dotted lines. The stars indicate where the pressure gradient S reaches Bi; the small circles indicate where the cell first becomes blocked (S reaches $\mathrm{B_w}$ for $\Sigma > 0$, or Bi for $\Sigma = 0$).

stress declines sufficiently to either side of the finger that S falls below Bi there (at the time indicated by the blue star in figure 6(c)). The fluid over these portions of the cell then deforms entirely as a sliding pseudo-plug.

The second case, shown at the bottom of figure 6(a), has a different value for Σ, such that the fluid purely slides in uniform withdrawal (*i.e.* $\mathrm{B_w} < S_0 < \mathrm{Bi}$). The development of an unstable finger, however, now raises the stress near the finger tip such that the fluid eventually fully yields internally there. The red star in figure 6(c) indicates the moment that internal yielding first arises.

For the solutions shown in figure 6, the solution for the pressure gradient over the nearly blocked parts of the cell becomes particularly sensitive to the spatial resolution and the regularization parameter ε. We cannot, therefore, reliably identify any rigid regions, or the detailed shape of any yield surfaces where $S = \mathrm{B_w}$. Nevertheless, the computations suggest that the yield stress is reached at the leftmost point of the interface close to the end of both computations in figure 6) (at the times indicated by the filled circles). Before this happens, the computations do reliably indicate relatively low fluxes to the left of the cell, as highlighted by the contours where $Q = 0.1$ that are also indicated in figure 6(a). The shape of these contours is more like the yield surfaces presented by Alexandrou & Entov, which might be due to the similarity between the two flux-gradient relations when $S < \mathrm{Bi}$.

Although the solutions with slip in figure 6 suggest that the fluid may block the cell at late times, the plugs appearing in the solution without sliding (figure 4(a)) are rather more pronounced. In particular, reliably detected plugs and yield surfaces arise without slip, with the stress certainly falling below the yield point well before the computation in figure 4 terminates. By contrast, with slip the pressure gradient declines more gradually (see figure 6(c)), but a better numerical scheme is called for to determine the late-time behaviour.

4. Circular interfaces and experiments

4.1. Experimental details

Our experimental arrangement consists of a cell formed by two plates of acrylic separated by spacers. We considered gaps of thickness $\mathcal{H} = 1.7$mm, 3.3mm and 4.7mm. Fluid or air could be pumped into or out of the cell through a pipe connected to a hole drilled into the lower plate. Pump rate $\mathcal{Q}$ varies from 5ml/min to 100ml/min. Additional acrylic sheets or weights were placed above the spacers to help maintain the uniformity of the gap and reduce any deformation of the plates. The fidelity of this arrangement was verified by monitoring the axisymmetry and radial advance of Saffman-Taylor stable displacements through the cell. The acrylic walls were either left in their smooth original state or roughened by 60 grit sandpaper to try to eliminate any effective slip. The hole through which fluid was pumped had a radius of $r_v = 2.75$mm for roughened cells, or $r_v = 3.8$mm for smooth the cells.

For the experimental fluid, we used aqueous suspensions of Carbopol (Ultrez 21, neutralized with sodium hydroxide, corresponding to an example of one of the suspensions used and reported by [38]; concentration 0.13% and density $\rho \approx 1\mathrm{g/cm^3}$). Throughtout the experiments we used three different solutions made up to this concentration. A Herschel-Bulkley fit of the flow curves measured in a rheometer (Kinexus Malvern fitted with roughened parallel plates) gave average rheological parameters of

$$\tau_{_Y} = 7.0 \pm 0.3 \text{ Pa},\ K = 5.3 \pm 0.1 \text{ Pa s}^{n-1},\ n = 0.42 \pm 0.01. \tag{51}$$

Figure B.16 in Appendix B compares flow curves with the Herschel-Bulkley fit. Some other experiments using corn syrup (viscosity 8.2 Pa s; density $1.4\,\mathrm{g/cm^3}$) are reported in Appendix A.

As illustrated in figure 1 we explore two versions of the Saffman-Taylor problem: the fingering of a retreating circular interface either on the outside of an extracted disk (panel (b)) or the inside of an expanding annulus (panel (c)). Both experiments begin by emplacing an initial disk of Carbopol in the cell; the advancing interface of this disk always remained stable. For the extracted disk, the pump was then reversed; for the annulus, the feeder pipe was exchanged for another that delivered a constant flux of air into the cell. A camera position above the cell recorded images of the air-Carbopol interfaces, which were then digitized by image processing (see the inset images in figure 1). The first images are taken a short time after pumping is initiated in order to avoid any start-up effects and to allow the inner interface to expand beyond the vent for the annulus tests. The experiments have three variable parameters: the volume of the initial disk V_{init}, the cell gap $\mathcal{H}$, and the pump rate $\mathcal{Q}$.

From the recorded interfaces we extracted the areal footprint of the Carbopol and translated this to the volume V within the cell (for comparison with that expected from the flux $\mathcal{Q}$). We further measured the instantaneous radius $R(\vartheta, t)$, expressed in terms of an angular variable, $\vartheta = 2\pi s/s_{_T}$, based on the ratio of the local arc length, s, to the total arc length, $s_{_T}$. We break this periodic variable down into its Fourier series to consider each angular mode, and use the scaled standard deviation,

$$S_{_R} = \sqrt{\langle (R/R_{av} - 1)^2 \rangle}, \tag{52}$$

as a convenient measure of the strength of the fingering instability, where the angular brackets indicate the average over ϑ. The variable ϑ is not equal to the polar angle θ, but avoids the problems that develop once the fingers become nonlinear and render the radius a multi-valued function of θ. Moreover, in the linear regime, ϑ and θ are equivalent.

4.2. Viscoplastic fingers and the impact of slip

Sample results for fingers forming on the retreating interface of an expanding annulus and extracted disk are presented in figures 7 and 8, respectively. In both cases,

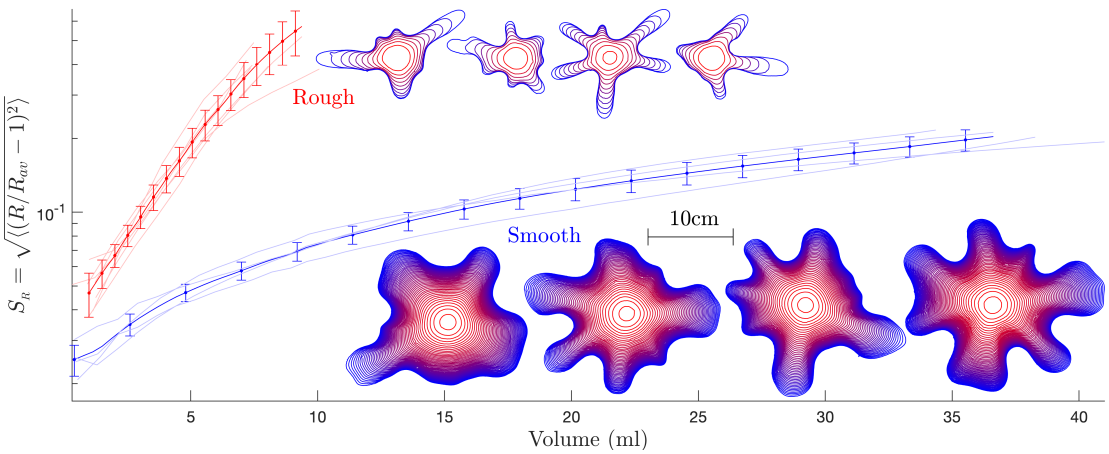

Figure 7: Repeated experimental tests for expanding annuli in cells with either rough or smooth plates, plotting the standard deviation of the radius $S_R = \sqrt{\langle (R/R_{av} - 1)^2 \rangle}$ against the volume V of air in the cell. For the rough cell, the test is repeated seven times; for the smooth cell, the test is repeated four times. The fainter lines show the individual tests; the average, with errorbars based on the standard deviation, are shown with darker lines. For both cells, outlines of the interface are shown for four sample tests. Parameters: $\mathcal{H} = 1.7$mm, $V_{init} = 50$ml and $\mathcal{Q} = 53$ml/min for rough plates or $\mathcal{Q} = 45$ml/min for smooth plates. The outlines are all separated by one second.

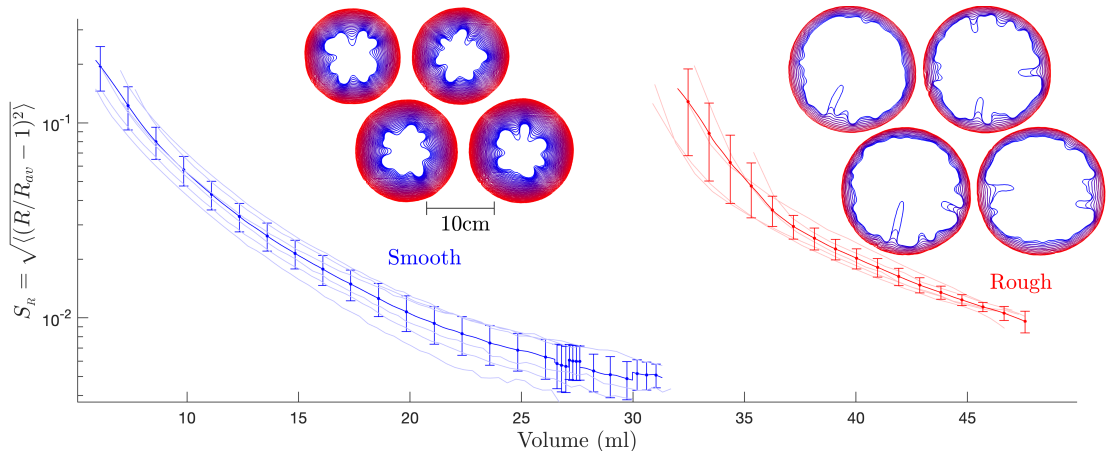

Figure 8: A similar plot to figure 7, but for experimental extractions of a disk, and for the volume V of Carbopol in the cell. The tests are repeated five times in the rough cell and six times in the smooth cell. Parameters: $\mathcal{H} = 1.7$mm, $V_{init} = 50$ml, and $\mathcal{Q} = 45$ml/min for rough plates and $\mathcal{Q} = 23$ml/min for smooth plates. The outlines are all separated by one second.

time series of the diagnostic in (52) are shown, along with sample series of outlines of the unstable interface, for both smooth and roughened cells. The retreating interface loses its initial axisymmetry after a short period, developing the distinctive fingers of the Saffman-Taylor instability. The tests are halted when the longest finger approaches either the outer air-Carbopol interface (for the annulus), or the vent (for the extraction). For the former, the outer interface largely maintains its axisymmetry until shortly before the longest finger breaks through it (*cf.* figure 1(c)).

A main conclusion that one immediately draws from figures 7 and 8 is that the development of the instability is very different in rough and smooth cells, a feature that must be due to effective slip. In particular, the fingers develop significantly more rapidly in the rough cells. Once formed, the fingers also lengthen faster in the roughened cells, with the rearward sections of the interface barely moving at late times; by contrast, in the smooth cells, the entire interface looks to remain in motion (*cf.* §3.2.2 and 3.2.3). These features are illustrated further in figure 9, which shows the advance of all the tips and roots of the fingers (*i.e.* the local radial maxima and minima of the interface) detected in the annulus experiments shown in figure 7.

The finger pattern arising in the experiments is never the same if the test is repeated, as illustrated by the sample interface outlines shown in figures 7 and 8. For example, for the experimental conditions used in the tests of figure 7, between 4 and 7 fingers appear on the interface of the expanding annulus in the rough cells; between 7 and 9 fingers appear on the interface in the smooth cells. The fingers typically have different strengths and angular positions relative to one another between tests (confirming the uniformity of the gap). We attribute the variability in the finger patterns to the impact of minor differences in the initial conditions, which prompts the growth of a

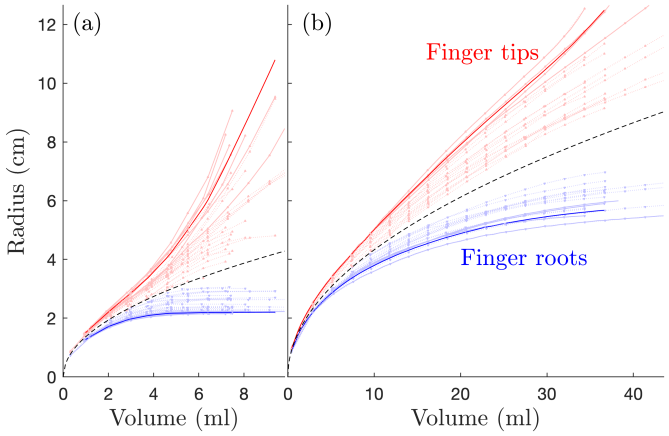

Figure 9: Experimental time series of the local, radial maxima and minima (the finger tips and roots) for the tests of figure 7, with the results for rough plates in (a), and those for smooth plates in (b). The fainter dotted lines and symbols show all the extrema (above a threshold level exceeding the noise in the original images); the lighter solid lines show the global maxima (red) and minima (blue). The darker solid lines show the averages over all the repeated tests, and the black dashed line is $R_{av}(t)$.

different selection of the unstable angular Fourier modes.[1] In order to reduce the impact of this variability on the diagnostics we employ to characterize the finger patterns, tests are repeated a number of times (typically between three and seven times), and the results are averaged over these repetitions (see figures 7 and 8).

4.3. Trends

The effect of the initial emplaced volume V_{init} is illustrated for annulus experiments in roughened cells in figure 10. Relatively small initial disks ($V_{init} = 5$ or 10ml) develop fingers that amplify sharply and quickly break through to the outer edge. However, increasing the initial volume above about 25ml leads to finger patterns that develop in much the same manner, except near the final moments when the longest finger breaks through. Indeed, for $V > 25$ml, the variation in the time series of the diagnostic (52) with V_{init} observed in figure 10 is less than the variability seen between the seven repetitions of the $V = 50$ml tests in figure 7 (as indicated by the error bars for that case). There is also no obvious trend in figure 10 for $V_{init} > 25$ml. Such observations therefore led us to take $V_{init} = 50$ml for the remainder of the experiments (corresponding to an initial radius of about 10cm in the cell with a gap of $\mathcal{H} = 1.7$mm) and otherwise ignore this parameter.

Trends with varying gap size and flux are illustrated for annulus experiments with rough and smooth cells in figure 11. The most significant variation is with cell size, with any increase in $\mathcal{H}$ significantly reducing the number

[1] In a few cases, the angular positions of the fingers do repeat between tests, suggesting spatial imperfections; this effect largely appears to be unimportant.

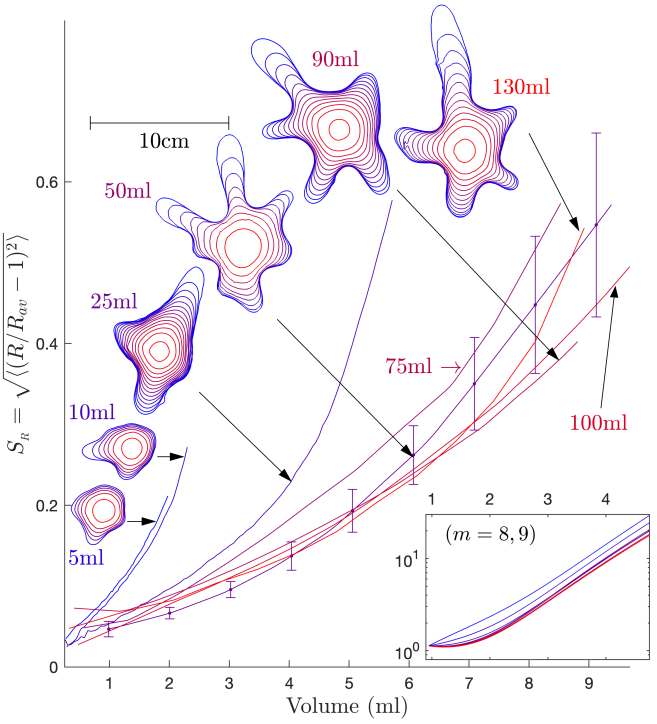

Figure 10: Expanding annuli experiments in roughened cells with different initial volumes V_{init} (as indicated), showing the standard deviation of the radius S_R against the volume V of air in the cell, plus sample outlines of the interface. Each test is conducted at least three times, except for the test with the largest initial annulus, which was conducted only once. The inset shows corresponding predictions of the linear stability theory, assuming an initial spectrum with $\hat{R}_m(0) = m^{-\frac{3}{2}}$. The most amplified mode has wavenumber $m = 8$ or 9. Parameter settings: $\mathcal{H} = 1.7$mm, with $\mathcal{Q}$ increasing monotonically from 41ml/min for the smallest V_{init} up to 68ml/min for the largest initial volume. Time difference as above.

of the fingers and their strength (figure 11(a)). The effect of varying flux is less dramatic for rough plates in figure 11(b), with the most obvious trend being that a single finger dominates more quickly as the flux is lowered. The highest flux with smooth plates displays a stronger instability, but the lower fluxes again remain comparable.

4.4. Comparison with linear theory

To complement the experiments we solve the linear stability problem in circular geometry. Because the base state is time-dependent, a normal-mode analysis of the kind outlined in §3.1 is not valid. Instead, we solve the linear equations as an initial-value problem after breaking down the problem into each angular Fourier mode with wavenumber m, and considering separately the paired interfaces of the expanding annulus or the single interface of the extracted disk (see [14]).

Given an initial spectrum for the linear, angular Fourier modes, one could also formulate suitable superpositions for a direct comparison of theory and experiment. However, as the initial states in the experiments project randomly onto these modes, formulating such an initial spectrum is

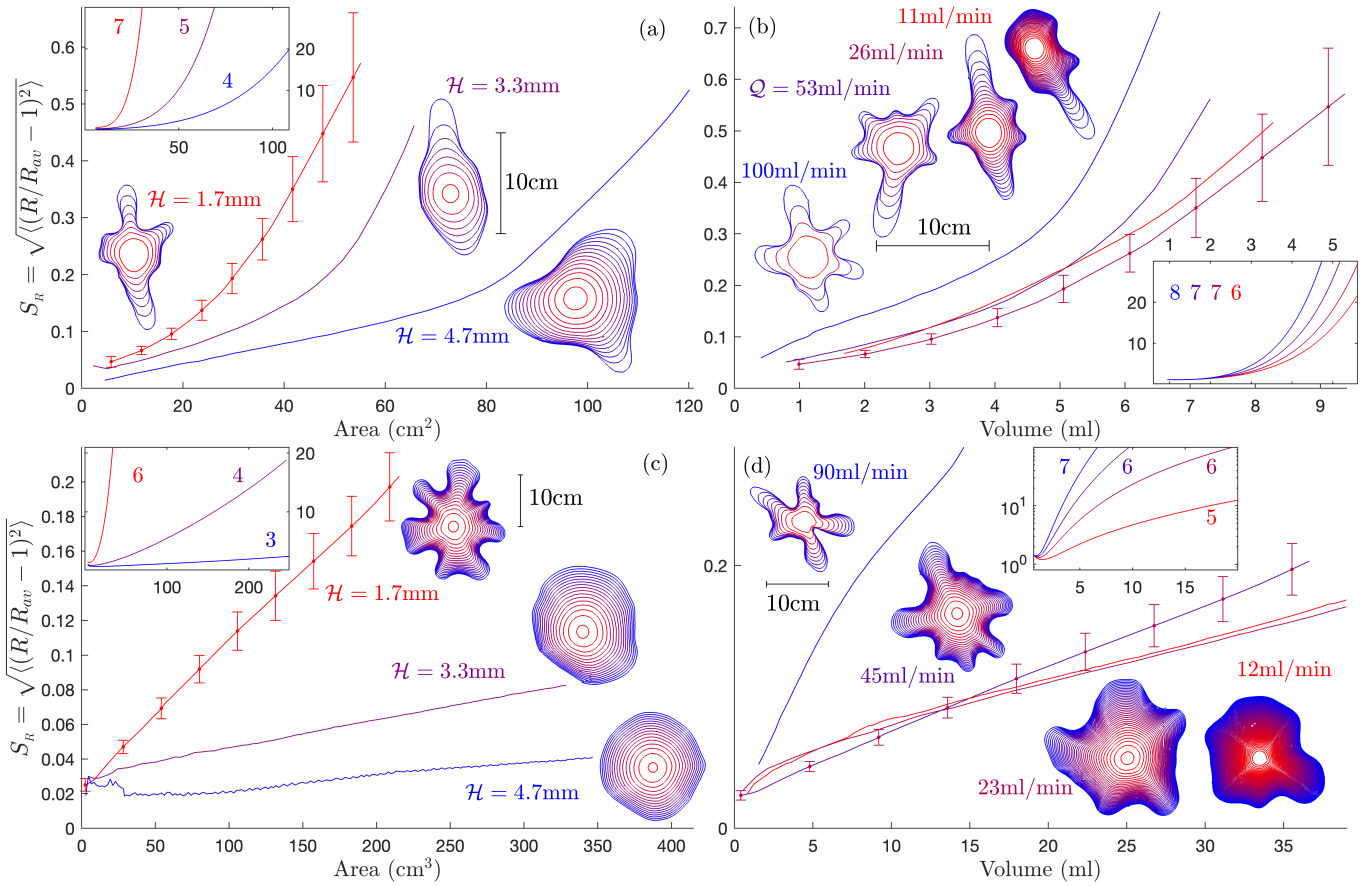

Figure 11: Expanding annuli experiments with different (a,c) gap size ($\mathcal{Q} = 53$ml/min in (a), 45ml/min in (c); $V_{init}/\mathcal{H} = 294$cm^2), and (b,d) flux ($\mathcal{H} = 1.7$mm, $V_{init} = 50$ml), as indicated. For (a,b) the plates are roughened; in (c,d), the plates are smooth. The diagnostic $S_R(t)$ is plotted against area, $V/\mathcal{H}$, in (a,c) and volume, V, in (b,d). The insets show the predictions of linear stability theory for the same gaps and fluxes (holding all other parameters fixed in each case), assuming an initial spectrum with $\hat{R}_m(0) = m^{-\frac{3}{2}}$. The numbers indicate the angular wavenumber m of the most amplified mode at the end of each time series.

challenging, particularly since the experimental Fourier series are contaminated by noise and image-processing artefacts. The theoretical model also features a relatively crude treatment of the interface that likely introduced order-one discrepancies (*cf.* [1, 2, 37]) and renders suspicious any detailed quantitative comparison with experiment. Consequently, we opt for a more qualitative comparison.

More specifically, we first observe that the Fourier series of $R(\vartheta, t)$ for the first snapshot of the interface is approximately given by a power-law $m^{-\frac{3}{2}}$ over the range $1 < m < 33$ (the best fit exponent is -1.41) for both the annulus and extraction experiments (see figure 12). We then use this spectrum to initialize the modes in the linear stability analysis, adopt the Herschel-Bulkley fit in (51), match the average radius of the first snapshot $r_o = \mathcal{L}$ and the experimental parameters, $(\mathcal{Q}, \mathcal{H}, V_{init})$, and assume that the surface tension is that of water (*cf.* [39, 40]). For the comparison with tests in roughened Hele-Shaw cells, we assume that the roughening the plates fully removes any effective slip. For the tests with smooth cells, we adopt the wall-slip model outlined in §2.1 with pa-

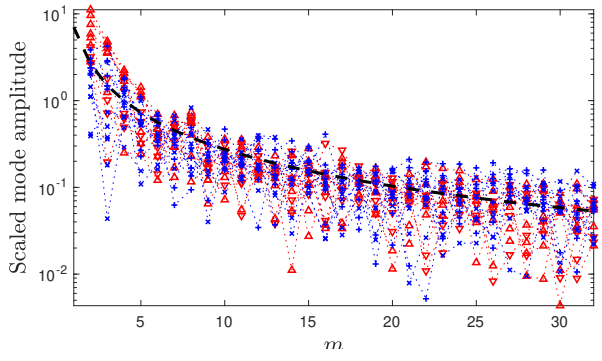

Figure 12: Fourier mode amplitudes experimentally observed for the first snapshots of the tests shown in figures 7 (red) and 8 (blue), for both rough and smooth plates. The modes are scaled by the power in modes $5 < m < 33$, and the dashed lines shows $m^{-\frac{3}{2}}$.

rameters $A = 1.56 \times 10^4$ Pa s m^{-1} and $\tau_{_W} = 0.18\tau_{_Y}$, guided by the calibrations of [18] (although those calibrations do not correspond precisely to the experimental conditions or fluids that we use here). All this translates to dimensionless parameter settings of $(\mathrm{Bi}, \sigma, \Sigma, \mathrm{B_w}) = (0.31, 0.014, 0, 0.057)$ and $(0.29, 0.028, 0.21, 0.051)$, for the rough and smooth plates of figure 7 (respectively), or $(\mathrm{Bi}, \sigma, \Sigma, \mathrm{B_w}) = (0.75, 7.1 \times 10^{-4}, 0, 0.135)$ and $(0.9, 1.3 \times 10^{-3}, 1, 0.16)$, for those of figure 8.

Figure 13 presents amplification factors, $|\hat{R}_m|/R_0(t)$ as densities over the $(V, m)-$plane for the experiments of figures 7 and 8. Here, generalizing §3.1, we set $R = R_0(t) + \hat{R}_m(t)e^{im\theta}$ for the perturbed unstable interface in the linear stability analysis, where $r = R_o(t) = \sqrt{1 \pm 2t}$ is the (dimensionless) unperturbed position. When a single mode is excited, this amplification factor corresponds to $S_{_R}(t)/S_{_R}(0)$.

For the annulus experiments in figure 13(a,b), the linear theory predicts that the most amplified modes are similar to those seen experimentally. Roughened cells are also predicted to be rather more unstable than smooth cells in line with the arguments in §3.1, numerical observations [7] and experimental observations of displacements of viscoplastic foams [4]. Despite this qualitative agreement, the amplifications predicted theoretically are rather higher than those seen experimentally (by a factor of ten or so), as found previously for Newtonian Saffman-Taylor fingering [41]. For the smooth cells, the most amplified modes are predicted to be higher in wavenumber than seen experimentally, and for rough cells the amplifications are again about ten times too high.

One possible explanation for the discrepancy in amplification factor is that the finger patterns do not remain in the linear regime for the duration of the experimental time series (*cf.* [41]). However, a more likely explanation is that the theory systematically overestimates the degree of growth in the higher wavenumbers, as we highlight in figure 14. This figure compares a selection of experimental Fourier mode amplitudes with theoretical predictions for the experiments of figures 7 and 8. Although comparisons of this kind are often obscured by experimental variability, some of the tests show satisfying repeatability (*e.g.* the mode $m = 3$ in figure 14(a), with relatively low error bars). Moreover, one sees clearly in figure 14 that the theoretical amplification factors are consistent with observations for the lower modes. Once the angular wavenumber reaches $m = 6$ or higher, however, the theory overestimates growth, a feature that becomes steadily worse until surface tension cuts off the range of growing wavenumbers. This overestimation is not only a property of the viscoplastic fingering problem: as we show in Appendix A, the experiments that we conducted with corn syrup also demonstrate the same discrepancy. Therefore, the issue may well point to a limitation of the Hele-Shaw approximation for our experiments (which is not altogether surprising in view of our simplistic treatment of the interface).

Note that the third case in figure 14, for extractions in roughened cells, has amplification factors that are almost exponential (on this semi-logarithmic plot, the dashed lines are almost straight), because the radius of the interface does not vary by much throughout the tests. The planar linear stability analysis of §3.1 therefore applies approximately, with $\ell \approx m$. For the other experiments, the curvature of the amplification factors emphasizes the time-dependent axisymmetric state.

Because the theory probably overestimates the growth of high wavenumbers, diagnostics of the kind in (52) are inevitably also overestimated. Nevertheless, we continue with this diagnostic to explore whether the trends observed experimentally in §4.3 can be broadly reproduced by the model. The predictions of this analysis for the annulus tests (varying one of $(V_{init}, \mathcal{H}, \mathcal{Q})$ whilst fixing the others) are included as insets in figures 10 and 11. The agreement is qualitative, if not quantitative, barring the sharp upturns in $S_{_R}(t)$ at the end of the experiments where the longest finger is about to break through the outer interface. The trends in initial volume are similar to those observed in weakly-nonlinear analysis and nonlinear simulations for displacement of a Newtonian annulus [42, 43]. However the trends with varying flux are less well captured. Despite this, the most amplified modes predicted by the linear stability analysis are, once more, in fair agreement with the trends in the observed numbers of fingers. This is consistent with observations from separating plate experiments [8, 13] and planar Saffman-Taylor experiments [4, 5] that show agreement with the theoretical wavelength of the most unstable mode in §3.1 (*cf.* [3]).

Note that model results for smooth plates in figures 11, 13 and 14 predict that the fluid deforms mostly by both sliding and internal shear. Only in the test with the lowest flux in figure 11(d) does a significant fraction of the fluid eventually fall below the internal yield criterion given by $S = \mathrm{Bi}$ (*cf.* figure 2). In particular, this arises for radii that are about four times the initial position of the inner interface.

5. Conclusion

In this paper we have provided a theoretical and experimental study of Saffman-Taylor fingering in a yield-stress fluid displaced in a Hele-Shaw cell by a weakly viscous fluid. The theory adopts the conventional Hele-Shaw approximation, generalized to account for both the yield-stress rheology and the possibility that effective slip takes place at the cell walls. Roughened cells, assuming that slip is removed, are predicted to be more prone to instability than smooth ones (with slip). Such a significant effect of slip is similar to that observed for displacement flows in channels by Taghavi [44]. Without slip and for low flow speeds (corresponding to the plastic limit), planar, nonlinear viscoplastic Saffman-Taylor fingers are predicted to achieve a width set by $\sqrt{\sigma_* \mathcal{H}/\tau_{_Y}}$ (where σ_* is the surface tension, $\tau_{_Y}$ the yield stress and $\mathcal{H}$ the thickness of

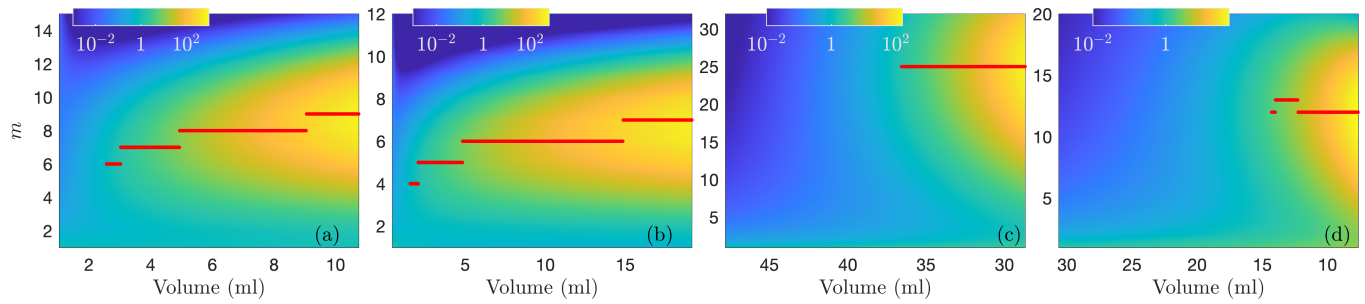

Figure 13: Linear stability numerical predictions for the amplification factors, $|\hat{R}_m|/R_0(t)$, of the angular mode m when the volume within the unstable interface is V. Panels (a,b) correspond to the annulus experiments of figure 7, for the rough and smooth cells, respectively (c,d) correspond to the extractions in rough and smooth cells in figure 8. The red points indicate the most amplified mode for $m > 1$.

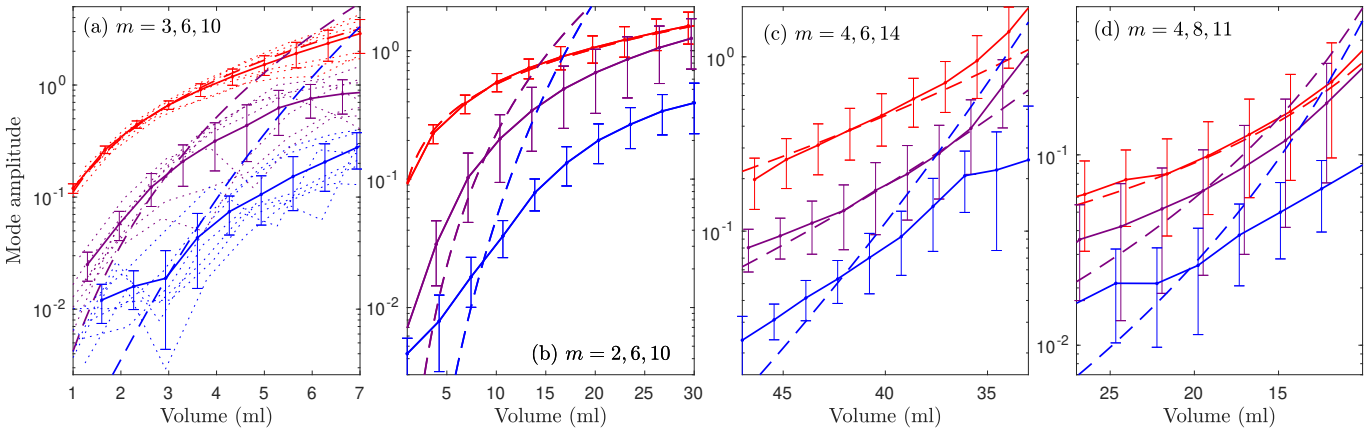

Figure 14: Experimentally observed and numerically predicted mode amplitudes $|\hat{R}_m|/R_0$, for the angular wavenumbers m indicated (colour coded from red to blue for increasing m). The experiments correspond to those in figures 7 and 8, and the panels are laid out as in figure 13. The solid lines and error bars show the average, plus or minus the standard deviation, of the repeated tests; in (a), the dotted lines show the results for each test. The dashed lines are the theoretical predictions, scaled to match the observed averages at a particular volume.

the cell), in agreement with the wavelength of the most unstable mode [3]. To either side of the advancing finger, the yield stress arrests flow, blocking the cell there. With slip, the blockages are less severe.

Our experiments were conducted by displacing suspensions of Carbopol with air in the circular geometries of an expanding annulus or extracted disk. The Hele-Shaw cells were made using acrylic plates. For a comparison with theory assuming no slip, we roughened the acrylic walls with sandpaper. Other techniques have been employed to remove slip, such as treating the surfaces chemically [45]. Here, however, we aimed for a relatively simple and robust technique, roughening the plates to mimic the process used in complementary rheometry.

To compare with the theoretical results incorporating a model for effective slip, we left the acrylic plates in their original smooth state, matching earlier experiments with measured slip parameters [18]. We also conducted some tests in which we applied a hydrophobic treatment to the plates to try to approach the opposite extreme and promote slip yet further. These tests were less successful, however, the interaction of the surface treatment with the Carbopol leading to spatially variable slip properties. Exploring the dynamics of yield-stress fluids on super-hydrophobic surface is certainly worthy of further exploration.

Our comparisons of theory and experiment were based on the evolving angular Fourier spectra, the number of fingers and their length. These measurements were taken starting a short while after each test commenced in order to minimize the influence of any initial transients or entrance effects at the feeder pipe. At this initial moment, the Fourier mode amplitudes were observed to take a power-law dependence on angular wavenumber, a feature that guided the initialization of corresponding linear stability computations. The modes subsequently evolved independently (at least until late times when the fingers significantly distorted the basis axisymmetrical flow), with different wavenumbers amplified most strongly at different times. In other words, the dynamics was linear, and the most unstable mode changed with time. The precise finger pattern was not therefore imprinted at the commencement of each experiment (supporting our strategy for discarding initial transients and entrance effects), and the observed initial spectrum facilitated a mode-by-mode comparison with linear stability theory.

In agreement with theoretical predictions, fingering in roughened cells was rather more pronounced than in

smooth cells, a feature that must be due to wall slip. Also in accord with the linear theory, fingers were wider in thicker cells, but insensistive to flux (see §4.3 and figure 11). Despite the relatively crude treatment of the interface in the theory, the amplification rates of the lower angular wavenumbers observed in the experiments match theoretical predictions fairly well; the growth of higher wavenumbers is overpredicted theoretically.

One could also advance beyond linear theory and try to establish connections between the experiments and the nonlinear finger computations. However, for our nonlinear analysis, we chose a surface tension parameter such that only the first Fourier mode was unstable. This choice eliminates any finger interactions, which limits the comparison with experiments. Nevertheless, by studying a single finger, we were able to compute the nonlinear dynamics accurately and demonstrate some qualitative agreement with the experiments. In particular, in roughened cells the lagging interface between nonlinear fingers largely came to rest, in agreement with experimental observations.

However, this conclusion is not obviously relevant to applications involving flow in porous media, where the tortuosity of the pore space could prevent slip occurring. In these situations, the inertial effects that we neglected may become more relevant at higher volume fluxes. The asymptotic nature of the model is lost when incorporating such terms in the theory; we leave this extension for future work.

Appendix A. Experiments with corn syrup

We also conducted a brief suite of experiments using expanding annuli of corn syrup (a Newtonian fluid with a viscosity of about 8.2 Pa s and initial volume $V_{init} = 50$ml) in a cell with gap $\mathcal{H} = 3.3$mm and flux $\mathcal{Q} = 59$ml/min. Because this fluid satisfies a no-slip condition on the plates, we took this opportunity to modify the manner in which we initiated each experiment and control more carefully the shape of the finger pattern. In particular, by adding small pieces of tape to one of the plates at certain locations close to the vent, we introduced an array of localized protrusions with a given angular spacing designed to kick a particular Fourier mode. This device was less successful when using Carbopol, as in the experiments of §4, because we mostly used roughened plates to remove effective slip, and the protrusions then had little effect.

Figure A.15 show the results from tests kicking modes $m = 3$ to 9, as well as a control experiment in which no protrusions were placed in the cell. As can be seen from the top row of snapshots of the evolving interface, the finger patterns kicked by protrusions with $m = 6$ to 8 largely maintain that angular symmetry until the end of each test. By contrast, the patterns kicked with lower wavenumber ($m = 3$ to 5) lose that symmetry as the interface expands, generating additional fingers; that perturbed with $m = 9$ becomes distorted by the growth of lower wavenumbers. Thus, for these particular experimental parameters, it appears that wavenumbers over the range $5 \leq m \leq 8$ are preferred, in line with the shape of the interface developing in the test without protrusions.

The plots in figure A.15 also break the interface shape, $r = R(\vartheta, t) = \sum_m \hat{R}_m(t) e^{im\vartheta}$, down into the lower Fourier modes with $3 \leq m \leq 9$. Even though each of the tests is kicked differently by the protrusions, these individual modes grow at largely the same rate and differ mainly in initial amplitude (as highlighted in the plots, where the mode amplitudes are scaled to align the data at an intermediate volume), except when they reach appreciable amplitude, or are obscured by noise. Consequently, the diagnostic $S_{_R}(t)$ in (52) also differs largely by a purely multiplicative factor. Notable exceptions to this rule are modes that are excited initially with relatively low amplitudes (and become impacted by noise), and the $m = 3$ and 4 modes of the first test, which rapidly becomes overtaken by the $m = 6$ mode and thereafter decay, presumably as a result of nonlinear effects. Therefore, we conclude that the modes grow mostly in the linear regime, and the detail manner in which the interface is perturbed is significant only in selecting the initial amplitudes. As for the Carbopol experiments of §4, the first snapshot of the interface shows an initial distribution for those amplitudes that follows the power law $m^{-\frac{3}{2}}$, discounting the specially excited mode (see the inset panel in figure A.15).

Also included in the mode amplitude plots are the predictions of linear stability analysis. These predictions imply that the most amplified modes are $m = 6$, 7 and 8 (using $\hat{R}_m(0) \propto m^{-\frac{3}{2}}$), and match well with the observations for the lower modes ($m = 3$ to 5), but then increasingly overestimate growth at higher wavenumber. That feature, and how it again contaminates the prediction for $S_{_R}(t)$, mirror the results reported in the main text for Carbopol.

Appendix B. Flow curves

Figure B.16 plots the flow curves of three Carbopol suspensions used in the experiments described in the main text in section §4.

References

[1] P. G. Saffman, G. I. Taylor, The penetration of a fluid into a porous medium or Hele-Shaw cell containing a more viscous liquid, Proceedings of the Royal Society of London. Series A. Mathematical and Physical Sciences 245 (1242) (1958) 312–329.

[2] P. G. Saffman, Viscous fingering in hele-shaw cells, Journal of Fluid Mechanics 173 (1986) 73–94.

[3] P. Coussot, Saffman–Taylor instability in yield-stress fluids, Journal of Fluid Mechanics 380 (1999) 363–376.

[4] A. Lindner, P. Coussot, D. Bonn, Viscous fingering in a yield stress fluid, Physical Review Letters 85 (2) (2000) 314.

[5] N. Maleki-Jirsaraei, A. Lindner, S. Rouhani, D. Bonn, Saffman–Taylor instability in yield stress fluids, Journal of Physics: Condensed Matter 17 (14) (2005) S1219.

[6] J. V. Fontana, S. A. Lira, J. A. Miranda, Radial viscous fingering in yield stress fluids: Onset of pattern formation, Physical Review E 87 (1) (2013) 013016.

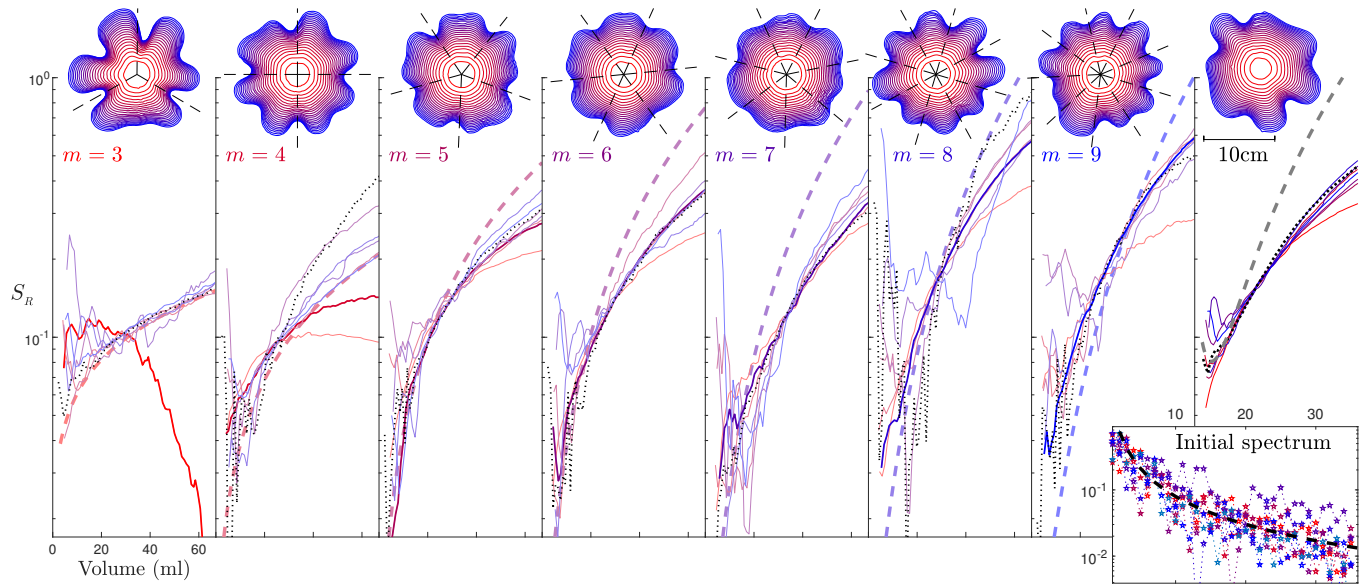

Figure A.15: Snapshots of expanding interfaces (top) and Fourier mode amplitudes of $R(\vartheta, t)/R_{av}(t)$ (bottom) for experiments with corn syrup. ($\mathcal{Q} = 59$ml/min, $\mathcal{H} = 3.3$mm, $V_{init} = 50$ml). Proceeding from the left to the penultimate column on the right (and colour coded from red to blue), the interface is perturbed initially by including small local protrusions in gap thickness arranged to excite modes with $m = 3$ to 9. In the mode amplitude plots, the thicker line shows the initially excited mode, and the dashed lines present the results of linear stability analysis, both scaled to align the data for some intermediate volume. The final column shows an experiment in which there were no such protrusions (with mode amplitudes identified by the black dotted lines in the other columns); the plot below shows the diagnostic $S_R(t)$ in (52), again scaled to an intermediate volume. The inset at the bottom right shows the initial mode amplitudes plotted against m for the first snapshot of each test; the dashed line indicates $m^{-\frac{3}{2}}$, the initial distribution that is used to compute the theoretical version of $S_R(t)$ immediately above.

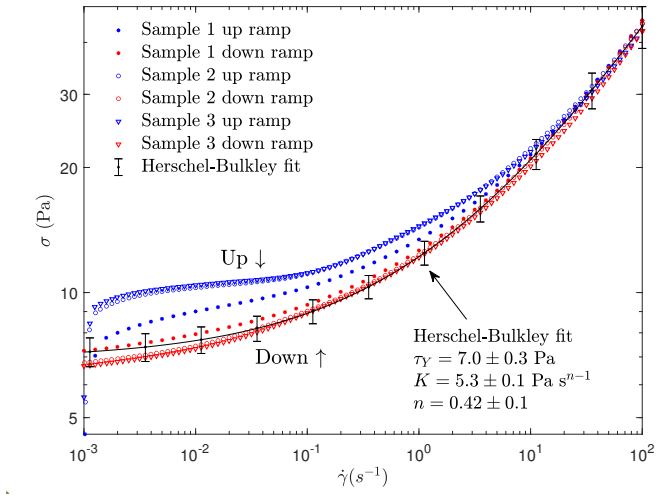

Figure B.16: The flow curves for the three aqueous suspension of Carbopol Ultrez 21, with a concentration 0.13% used in our experiments. The data was collected using a controlled shear-rate ramp on a Kinexus Malvern rheometer fitted with roughened parallel plates. The ramp up and down data are denoted by red and blue markers respectively. The solid black curves show the Herschel-Bulkley fit for the data on the down ramp.

[7] B. Ebrahimi, P. Mostaghimi, H. Gholamian, K. Sadeghy, Viscous fingering in yield stress fluids: a numerical study, Journal of Engineering Mathematics 97 (1) (2016) 161–176.

[8] O. A. Fadoul, P. Coussot, Saffman–Taylor instability in yield stress fluids: Theory–experiment comparison, Fluids 4 (1) (2019) 53.

[9] A. Eslami, S. M. Taghavi, Viscous fingering of yield stress fluids: The effects of wettability, Journal of Non-Newtonian Fluid Mechanics 264 (2019) 25–47.

[10] A. Eslami, S. M. Taghavi, Viscoplastic fingering in rectangular channels, Physical Review E 102 (2) (2020) 023105.

[11] D. Derks, A. Lindner, C. Creton, D. Bonn, Cohesive failure of thin layers of soft model adhesives under tension, Journal of applied physics 93 (3) (2003) 1557–1566.

[12] Q. Barral, G. Ovarlez, X. Chateau, J. Boujlel, B. Rabideau, P. Coussot, Adhesion of yield stress fluids, Soft Matter 6 (6) (2010) 1343–1351.

[13] T. Divoux, A. Shukla, B. Marsit, Y. Kaloga, I. Bischofberger, Criterion for fingering instabilities in colloidal gels, Physical Review Letters 124 (1) (2020) 248006.

[14] T. V. Ball, N. J. Balmforth, A. P. Dufresne, Viscoplastic fingers and fractures in a hele-shaw cell, Journal of Non-Newtonian Fluid Mechanics 289 (2021) 104492.

[15] S. H. Bittleston, J. Ferguson, I. A. Frigaard, Mud removal and cement placement during primary cementing of an oil well – laminar non-Newtonian displacements in an eccentric annular Hele-Shaw cell, Journal of Engineering Mathematics 43 (2-4) (2002) 229–253.

[16] D. R. Hewitt, M. Daneshi, N. J. Balmforth, D. M. Martinez, Obstructed and channelized viscoplastic flow in a Hele–Shaw cell, J. Fluid Mech. 790 (2016) 173–204.

[17] H. A. Barnes, A review of the slip (wall depletion) of polymer solutions, emulsions and particle suspensions in viscometers: its cause, character, and cure, Journal of Non-Newtonian Fluid Mechanics 56 (3) (1995) 221–251.

[18] M. Daneshi, A. Pourzahedi, D. M. Martinez, D. Grecov, Charac-

terising wall-slip behaviour of carbopol gels in a fully-developed poiseuille flow, Journal of Non-Newtonian Fluid Mechanics 269 (2019) 65–72.
[19] N. J. Balmforth, I. A. Frigaard, G. Ovarlez, Yielding to stress: Recent developments in viscoplastic fluid mechanics, Ann. Rev. Fluid Mechanics 46 (2014) 121–146.
[20] M. Daneshi, J. MacKenzie, N. J. Balmforth, D. M. Martinez, D. R. Hewitt, Obstructed viscoplastic flow in a hele-shaw cell, Physical Review Fluids 5 (1) (2020) 013301.
[21] N. J. Balmforth, R. V. Craster, A consistent thin-layer theory for Bingham fluids, J. Non-Newtonian Fluid Mech. 84 (1999) 65–81.
[22] Y. Liu, N. J. Balmforth, S. Hormozi, Viscoplastic surges down an incline, Journal of Non-Newtonian Fluid Mechanics 268 (2019) 1–11.
[23] N. J. Balmforth, R. V. Craster, D. R. Hewitt, Building on oldroyd's viscoplastic legacy: Perspectives and new developments, Journal of Non-Newtonian Fluid Mechanics 294 (2021) 104580.
[24] A. N. Alexandrou, V. Entov, On the steady-state advancement of fingers and bubbles in a Hele–Shaw cell filled by a non-Newtonian fluid, European Journal of Applied Mathematics 8 (1) (1997) 73–87.
[25] A. Oron, S. H. Davis, S. G. Bankoff, Long-scale evolution of thin liquid films, Reviews of modern physics 69 (3) (1997) 931.
[26] R. V. Craster, O. K. Matar, Dynamics and stability of thin liquid films, Reviews of modern physics 81 (3) (2009) 1131.
[27] D. R. MacAyeal, V. Barcilon, Ice-shelf response to ice-stream discharge fluctuations: I. unconfined ice tongues, Journal of Glaciology 34 (116) (1988) 121–127.
[28] D. R. MacAyeal, Large-scale ice flow over a viscous basal sediment: Theory and application to ice stream b, antarctica, Journal of Geophysical Research: Solid Earth 94 (B4) (1989) 4071–4087.
[29] N. J. Balmforth, Viscoplastic asymptotics and other analytical methods, in: Lectures on visco-plastic fluid mechanics, Springer, 2019, pp. 41–82.
[30] T. V. Ball, N. J. Balmforth, Instability of sliding viscoplastic films, Journal of Fluid Mechanics 912 (2021).
[31] S. D. R. Wilson, A note on the measurement of dynamic contact angles, Journal of Colloid and Interface Science 51 (3) (1975) 532–534.
[32] S. D. R. Wilson, The Taylor–Saffman problem for a non-Newtonian liquid, Journal of Fluid Mechanics 220 (1990) 413–425.
[33] C.-W. Park, G. M. Homsy, Two-phase displacement in Hele-Shaw cells: theory, Journal of Fluid Mechanics 139 (1984) 291–308.
[34] G. Tryggvason, H. Aref, Finger-interaction mechanisms in stratified hele-shaw flow, Journal of Fluid Mechanics 154 (1985) 287–301.
[35] A. J. DeGregoria, L. W. Schwartz, A boundary-integral method for two-phase displacement in hele-shaw cells, Journal of Fluid Mechanics 164 (1986) 383–400.
[36] J. W. McLean, P. G. Saffman, The effect of surface tension on the shape of fingers in a hele shaw cell, Journal of Fluid Mechanics 102 (1981) 455–469.
[37] E. Pitts, Penetration of fluid into a hele–shaw cell: The saffman–taylor experiment, Journal of Fluid Mechanics 97 (1) (1980) 53–64.
[38] T. V. Ball, N. J. Balmforth, A. P. Dufresne, S. W. Morris, Fracture patterns in viscoplastic gravity currents, Journal of Fluid Mechanics 934 (2022) A31.
[39] J. Boujlel, P. Coussot, Measuring the surface tension of yield stress fluids, Soft Matter 9 (25) (2013) 5898–5908.
[40] B. Géraud, L. Jørgensen, L. Petit, H. Delanoë-Ayari, P. Jop, C. Barentin, Capillary rise of yield-stress fluids, EPL (Europhysics Letters) 107 (5) (2014) 58002.
[41] D. Pihler-Puzović, G. G. Peng, J. R. Lister, M. Heil, A. Juel, Viscous fingering in a radial elastic-walled hele-shaw cell, Journal of Fluid Mechanics 849 (2018) 163–191.
[42] P. H. A. Anjos, S. Li, Weakly nonlinear analysis of the saffman-taylor problem in a radially spreading fluid annulus, Physical Review Fluids 5 (5) (2020) 054002.
[43] M. Zhao, P. H. Anjos, J. Lowengrub, S. Li, Pattern formation of the three-layer saffman-taylor problem in a radial hele-shaw cell, Physical Review Fluids 5 (12) (2020) 124005.
[44] S. M. Taghavi, A two-layer model for buoyant displacement flows in a channel with wall slip, Journal of Fluid Mechanics 852 (2018) 602–640. doi:10.1017/jfm.2018.555.
[45] C. Métivier, Y. Rharbi, B. Antoine, Stick-slip control of the carbopol microgels on polymethyl methacrylate transparent smooth walls, Soft Matter 8 (2012) ,7365. doi:10.1039/C2SM26244D.